symmetry

MDPI

Article

Dynamic Characteristics of a Segmented Supercritical Driveline with Flexible Couplings and Dry Friction Dampers

Zhonghe Huang [1], Jianping Tan [2,*], Chuliang Liu [2] and Xiong Lu [3]

[1] Light Alloy Research Institute, Central South University, Changsha 410083, China; huangzhonghe@csu.edu.cn
[2] State Key Laboratory of High Performance Complex Manufacturing, Central South University, Changsha 410083, China; liuchuliang@csu.edu.cn
[3] China Aviation Powerplant Research Institute, Zhuzhou 412002, China; hudaluxiong@163.com
* Correspondence: jptan@csu.edu.cn; Tel.: +86-188-9009-1853

Abstract: Helicopter tail rotors adopt a segmented driveline connected by flexible couplings, and dry friction dampers to suppress resonance. Modeling for this system can provide a basic foundation for parameter analysis. In this work, the lateral-torsional vibration equation of the shaft with continuous internal damping is established. The static and dynamic effects caused by flexible diaphragm couplings subject to parallel and angular misalignment is derived. A novel dual rub-impact model between the shaft and dry friction damper with multiple stages is proposed. Finally, a model of a helicopter tail rotor driveline incorporating all the above elements is formulated. Numerical simulations are carried out by an improved Adams–Bashforth method following the design flowchart. The dynamics of multiple vibration suppression, and the static and dynamic misalignment are analyzed to illustrate the accuracy and characteristics of the model. The coeffect of the rub impact and the misalignment on shafts and dampers are presented through the results of simulation and experiment. It provides an accurate and comprehensive mathematical model for the helicopter driveline. Response characteristics of multiple damping stages, static and dynamic misalignment, and their interaction are revealed.

Keywords: segmented supercritical driveline; flexible coupling; misalignment; dry friction damper; dual rub-impact

Citation: Huang, Z.; Tan, J.; Liu, C.; Lu, X. Dynamic Characteristics of a Segmented Supercritical Driveline with Flexible Couplings and Dry Friction Dampers. *Symmetry* **2021**, *13*, 281. https://doi.org/10.3390/sym13020281

Academic Editor: Juan Luis García Guirao
Received: 18 January 2021
Accepted: 1 February 2021
Published: 6 February 2021

1. Introduction

Tail rotor drivelines with the flexible diaphragm couplings of a helicopter transmit torque from the main gearbox to the tail rotor [1]. The driveline always adopts multiple segments with hollow thin-walled tube structures. It is frequently imposed on supercritical operating conditions [2,3]. When the shaft passes through the resonance region, excessive vibration can be avoided by using a dry friction damper [4]. The parameter configuration of the system needs a set of theoretical supports. The response characteristics of flexible multi-shafts connected by flexible diaphragm couplings subject to the misalignment are complicated and coupled with the unclear damping mechanism of dry friction dampers, which leads to a lack of theoretical support and deep insights into the dynamic behaviors of the system. The early stage of this damper design is mainly based on experience without adequate theoretical support, which brings about a degree of subjectiveness in the configuration of its parameters. Therefore, it is indispensable and crucial for this research to establish an accurate analytical model for the system, which can be used as a foundation for deep insights into dynamic behaviors.

Rotor dynamics play an important role in many engineering fields and have also been studied in a large number of investigations [5,6]. Fault recognition associated with complicated nonlinear vibrational behavior is a popular research topic in the literature [7–9]. With the development of artificial intelligence, machine learning and statistical framework are also applied in rotor dynamics [10,11]. The rotor–stator system described in most research is based on a lumped mass model, which is inappropriate for a slender shaft. For the case of slender systems, the finite element (FE) method is an available solution that many researchers have employed [12,13]. Q Han et al. developed an FE model for a shaft with a dual disk. The shaft was divided into Euler–Bernoulli beam elements with the consideration of all transverse DOFs (degrees of freedom) and gyroscopic effects of the discs for the rotor [14]. Hui Ma et al. established an FE model of the rotor system characterized by the shaft being discretized by Timoshenko beam elements after omitting the transnational and rotational DOFs [15]. M. A. addressed the FE modelling of a cracked rotor system with a transverse open crack [16,17]. Obviously, the lumped mass model is not suitable for multi-shafts with external components in the helicopter tail rotor driveline, while the FE method requires that many matrix manipulations of the distribution of the mass, flexibility, internal damping of the shaft, and movement of the ring are employed. Therefore, this paper will explore a new approach to establish a model for the helicopter tail rotor driveline that synthetically considers all kinds of factors.

The interaction between the shaft and the ring is similar to rub impact motion, which is widely acknowledged as a type of failure or fault. Nevertheless, it exists as a method of vibration reduction in dry friction dampers in this work. Even if rub impact is a classical research field of rotor dynamics, more in-depth and targeted investigations considering more factors in the rub-impact model combined with new research methods and ideas have been conducted by scholars [18,19]. Chunli Hua et al. established a mathematical model of the rotor-bearing system characterized by the nonlinear stiffness of a rubber bearing [20]. Lumiao Chen et al. developed a model between a rotating shell and stator, where the effects of the geometrical parameters and deformation angular position are taken into account [21]. Wen-Ming Zhang et al. presented a rub-impact micro-rotor model considering nonlinear scaling effects and friction coefficients due to adhesion forces in dry friction [22]. One can recognize that those investigations concentrate on the characteristics or special points of the model. However, to the best of the authors' knowledge, no work has been reported on the dual rub impact or dry friction damper with multiple stages. In this work, the dual rub-impact model between the shaft and damper consisting of the first process with variable DOFs and the second process with nonlinear stiffness is developed.

The impact stiffness directly affects the accuracy of the rub-impact model. The local surface stiffness of the metal stator at the collision point is generally regarded as the impact stiffness, while the remaining position is defined as the rigid body [23]. This stiffness is directly presented with subjectivity in most of the literature, but the process of acquiring it is critical to the accuracy of simulations. Only a few studies, for instance, by Guo Fa Zhang et al., divide rub impact into three types to explain the calculation of the stiffness between a metal stator and rotor [24]. Nonetheless, Chen, L et al. indicated that the impact stiffness should take into account the flexible deformation of the rotor made of the cylindrical shell [20]. Note that the stator flexibility should be employed in the impact stiffness between the sleeve and the ring in this work, as shown the structure of a dry friction damper in Figure 1. This is primarily because the stiffness of the ring made of polymeric materials is much smaller than that of the metal sleeve, and the ring can produce deformation once impacted with the sleeve. Efforts will be made to introduce how to obtain this parameter from practical dry friction dampers in this work.

Coupling or universal joints are used to connect the shaft, which can compensate for installation errors. The super harmonic nonlinear lateral vibration effect caused by universal joints subject to misalignment was initially demonstrated by experiments [25,26]. The model and instability region of the universal joint has been presented and simulated, showing the correlation with physical test results [27,28]. However, investigations on the dynamic characteristics of flexible coupling are relatively limited. Some investigations only analyze the dynamic characteristics caused by angle misalignment [29,30]. Some have investigated the coupling effect of parallel misalignment and angular misalignment of the connection of two rigid shafts [31,32]. In this work, the flexible coupling is used to connect the flexible drive shaft, so in addition to the flexibility of the coupling, the flexible deformation of the shaft should be considered as a factor. In addition, there is no vibration response analysis in the case of the coeffect of rub impact and misalignment in the current literature.

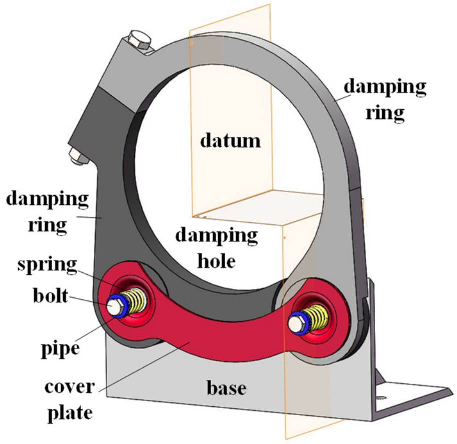

Figure 1. Structure of a dry friction damper.

This work provides a mathematical model for the parameter analysis of a segmented supercritical driveline with flexible couplings and dry friction dampers in a helicopter. Before the actual test of the helicopter driveline, the dynamic response obtained from the simulation analysis of the model proposed can be used to evaluate the rationality of parameter setting. The developed multi segment model also can be extended to segmented driveline, such as the transmission chain of some vehicles. Dual rub impact model provides a framework for some systems with rotor/nested stator.

This paper consists of six sections. After this introduction, the mathematical formulation for a multi-slender shaft with viscous internal damping and flexible coupling is established in Section 2. The damping features are introduced at the beginning of Section 3. The impact stiffness involving the deformation of the ring and local surface stiffness is investigated in Section 3.2.2. The rub impact model for multiple stages is developed in Section 3.2. Section 3.3 establishes equations of motion for the helicopter tail rotor driveline. Section 4 introduces the computational algorithm and simulation results based on the improved Adams–Bashforth method. The dynamic responses of rub impact and the misalignment effect of flexible diaphragm coupling are presented in Sections 4.1 and 4.2. The coeffect of misalignment and vibration suppression is investigated in Section 4.3. Experimental verification is conducted in Section 5. Finally, conclusions are drawn in Section 6.

2. The Mathematical Formulation for Segmented Helicopter Driveline with Flexible Coupling

Segmented helicopter driveline with flexible, intermediate, slender shafts, as given in Figure 2. The torque N is transferred from the input side to the output side. The middle reducer and tail inclined shaft are simplified as lumped inertia J. The shaft is rotating about the X-axis relative to the inertia-fixed coordinate frame XYZ. $X_rY_rZ_r$ is the rotating coordinate frame with X_r coinciding with X, while Y_r and Z_r rotate about the X_r axis at the same angular velocity as the shaft. $u(x,t), v(x,t), w(x,t)$ are dynamic deflection in the X, Y, and Z axial directions in the inertia-fixed coordinate system caused by the eccentricity of the shaft and external load produces. $u_s(x,t), v_s(x,t), w_s(x,t)$ are dynamic deflection in the rotating coordinate system. The torque and inertia induce twist are $\varphi_1(x,t), \varphi_2(x,t)$ along X. The shafts are connected with flexible diaphragm couplings.

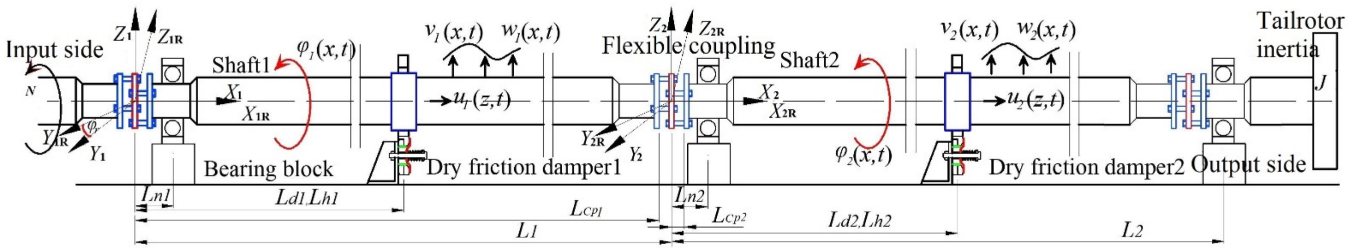

Figure 2. Profile of segmented supercritical driveline with flexible diaphragm couplings and dry friction dampers.

2.1. Slender Flexible Shaft with Viscous Internal Damping

The following reasonable assumptions are made: Due to the axial displacement limitation along the X-axis, $u(x,t) = u_{rt}(x,t) = 0$, $u(x,t) = u_{rt}(x,t) = 0$, are assumed. It is assumed that the rotation angle at any position of the intermediate shaft and output shaft are equal to that of the rotating coordinate since the inertia of the shaft is negligible compared to the tail lumped inertia J_L, and the speed variation caused by a misalignment between the shafts is small, i.e., $\varphi_1(x,t) = \varphi_2(x,t) = \varphi_r(t) = \Omega t + \phi(x,t)$. J and N can be moved to both ends of two intermediate shafts. The sleeve or disc in the shaft moves with the shaft segment, and its length is negligible relative to the shaft. According to the disk kinetic energy presented in ref. [5], the vibration kinetic energy expression for a sleeve or disc, or a short segment in the shaft, is

$$T_h = \tfrac{1}{2}m_h\left[\dot{v}^2(x,t) + \dot{w}^2(x,t)\right]\Big|_{x=Lh} + \tfrac{1}{2}\rho\left[I_{hz}\dot{v}'^2(x,t) + I_{hy}\dot{w}'^2(x,t)\right]\Big|_{x=Lh} + \tfrac{1}{2}I_{hx}\Omega^2 + \tfrac{1}{2}\rho I_{hx}\Omega\left[\dot{v}'(x,t)w'(x,t) - v'(x,t)\dot{w}'(x,t)\right]\Big|_{x=Lh} \quad (1)$$

The lateral energy of the shaft can be obtained by integrating Equation (1) along with the X-axis. In this case, $I_{hx} = 2I_{hz}$. Subscripts 1 and 2 are used to distinguish shaft 1 and shaft 2 or damper 1 and damper 2. Taking shaft 1 as an example, considering the torsional kinetic energy of shaft 1, the kinetic energy is obtained as follows

$$T_1 = \frac{1}{2}\int_0^{L_1} [\rho_1 A_1(\dot{v}^2(x,t) + \dot{w}^2(x,t)) + \rho_1 I_1(\dot{v}'^2(x,t) + \dot{w}'^2(x,t) + 2\rho_1 I_1\Omega(w'(x,t)\dot{v}'(x,t) - \dot{w}'(x,t)v'(x,t))]dx \quad (2)$$

where $(\cdot)$ and $(')$ denote differentiation concerning time and the X-axis, respectively. Internal damping (rotating damping) and external damping (nonrotating damping) are distinguished and introduced into this system. The dissipation energy and the strain energy of the shaft in the rotating coordinate frame can be rewritten as:

$$D_{rt1} = \frac{1}{2}\int_0^{L_1}\left\{c_{vi}E_1 I_1\left[\dot{v}''^2_{rc}(x,t) + \dot{w}''^2_{rc}(x,t)\right] + 2G_\phi I_1\dot{\phi}'_1(x,t)\right\}dx \quad (3)$$

$$V_{rt1} = \frac{1}{2}\int_0^{L_1}\left\{E_1 I_1\left[v''^2_s(x,t) + w''^2_s(x,t)\right] + 2G_\phi I_1\phi'_1(x,t)\right\}dx \quad (4)$$

Deflections and velocities in rotating frame coordinates are related to those in the inertia-fixed coordinate frame by

$$\begin{bmatrix} v_{rt} \\ w_{rt} \end{bmatrix} = \begin{bmatrix} \cos\varphi & \sin\varphi \\ -\sin\varphi & \cos\varphi \end{bmatrix}\begin{bmatrix} v \\ w \end{bmatrix} \begin{bmatrix} \dot{v}_{rt} \\ \dot{w}_{rt} \end{bmatrix} = \begin{bmatrix} \cos\varphi & \sin\varphi \\ -\sin\varphi & \cos\varphi \end{bmatrix}\begin{bmatrix} \dot{v} \\ \dot{w} \end{bmatrix} + \Omega_i\begin{bmatrix} -\sin\varphi & \cos\varphi \\ -\cos\varphi & -\sin\varphi \end{bmatrix}\begin{bmatrix} v \\ w \end{bmatrix} \quad (5)$$

Substituting Equation (5) into Equations (4) and (3), the dissipation and strain energy of the shaft in inertia-fixed coordinate can be rewritten as

$$V_1 = \frac{1}{2}\int_0^{L_1}\left\{E_1 I_1\left[v''^2(x,t) + w''^2(x,t)\right] + 2G_\phi I_1\phi'_1(x,t)\right\}dx \quad (6)$$

$$D_1 = \tfrac{1}{2}c_{vi}E_1 I_1\int_0^{L_1}\left\{\dot{v}''^2(x,t) + \dot{w}''^2(x,t) + 2\Omega\left[\dot{v}''(x,t)w''(x,t) - \dot{w}''(x,t)v''(x,t)\right] + \Omega^2\left[v''^2(x,t) + w''^2(x,t)\right] + 2G_\phi I_1\dot{\phi}'_1(x,t)\right\}dx \quad (7)$$

where c_{vi} is internal damping coming from the material of the shaft itself, and the viscous damping model is adopted in this work. External damping refers to damping at the bearing block, which absorbs the vibration of the shaft but does not rotate with the shaft. The bearing block is modeled as discrete damping and spring in the Z-Y direction. Thus, the bearing strain energy and dissipation function are written as

$$V_{n1} = \frac{1}{2}K_{n1}\left[(v(L_{n1},t)^2 + w(L_{n1},t)^2\right], D_{n1} = \frac{1}{2}c_{n1}\left[\dot{v}(L_{n1},t)^2 + \dot{w}(L_{n1},t)^2\right] \tag{8}$$

where L_{n1}, K_{n1}, c_{n1} are the axial location of the bearing block, equivalent spring stiffness, and damping, respectively.

The eccentricity of the shaft and disc are decomposed in the Z-Y direction:

$$\begin{array}{l} F_z(x,t) = e_1(x)\rho_1 A_1 \Omega^2 \cos(\Omega t), F_{hz}(L_h,t) = m_{e1}e_{h1}\Omega^2\cos(\Omega t) \\ F_y(x,t) = e_1(x)\rho_1 A_1 \Omega^2 \sin(\Omega t), F_{hy}(L_h,t) = m_{e1}e_{h1}\Omega^2\sin(\Omega t) \end{array} \tag{9}$$

where L_{h1}, m_{e1}, e_{h1} denote the location at the X-axis, eccentric mass, and eccentric distance of the disc or sleeve, respectively. $e_1(x)$ is the eccentricity of the shaft along the X-axis.

2.2. Flexible Diaphragm Couplings Subject to Misalignment

Hexagon diaphragm coupling is used to connect two shafts and can compensate for certain misalignments, as shown in Figures 3 and 4. O and O' are the centers of half-band coupling in shaft 1 and shaft 2, respectively. OOi is the initial parallel misalignment, and OO' is the parallel operating deviation. D, E and F are the fixing points of the three bolts in the half-band coupling of shaft 1 and the diaphragm, and A, B and C are the fixing points of the three bolts in the half-band coupling of shaft 2 and the diaphragm. Due to the parallel deviation, A, B, C move parallel to A', B', C'. R_{cp} is the distance from the diaphragm center to the bolt. φ_{Lcp} is the rotation angle of bolt hole A as it spins around central point O'. We have

$$q = OO' = \sqrt{(v_{cp}+v_{st})^2 + (w_c + w_{st})^2},\ \beta = \angle O'OX = \arctan\frac{v_{cp}+v_{st}}{w_{cp}+w_{st}} \tag{10}$$

where v_c, w_c are the dynamic parallel misalignment offsets and equal to the deflection difference of the two shafts along the Z and Y directions at couplings, i.e., $v_{cp} = v_1(L_{cp1},t) - v_2(L_{cp2},t), w_{cp} = w_1(L_{cp1},t) - w_2(L_{cp2},t)$, v_{st} and w_{st} are static parallel misalignment offsets. $\angle O'OA' = \pi + \beta - \varphi$ in the triangle $\Delta O'OA$, and based on the cosine theorem, we have

$$OA' = \sqrt{q^2 + {R_{cp}}^2 + 2qR_c\cos(\beta - \varphi_{Lcp})} \tag{11}$$

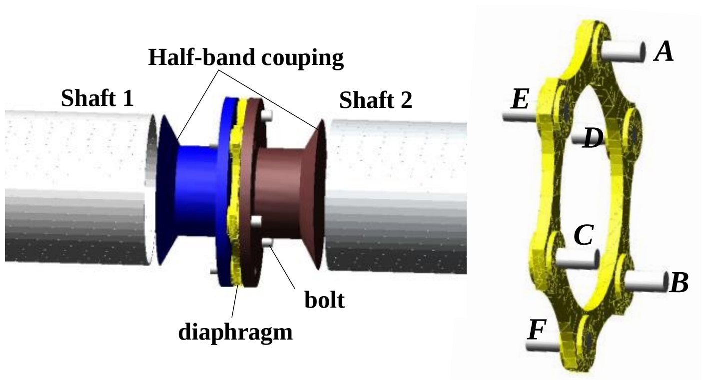

Figure 3. Structure of a flexible diaphragm coupling.

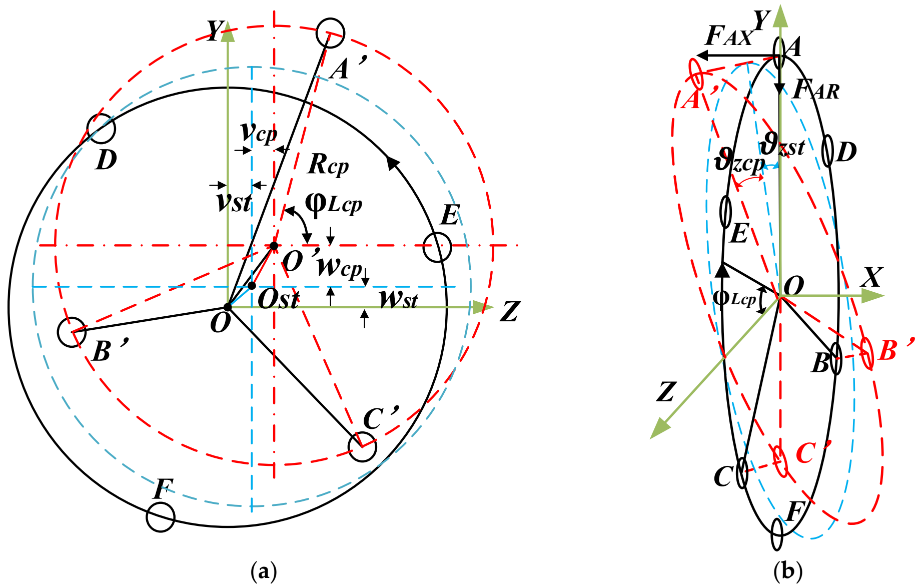

Figure 4. The layout of (**a**) parallel and (**b**) angular misalignment.

Similarly, since $\angle O'OB' = \pi/3 + \beta - \varphi$, then we have

$$OB' = \sqrt{q^2 + R_{cp}{}^2 - 2qR_{cp}\cos(\frac{\pi}{3} + \beta - \varphi_{Lcp})} \tag{12}$$

$\angle O'OC' = \pi/3 + \varphi - \beta$, then one obtains

$$OC' = \sqrt{q^2 + R_c{}^2 - 2qR_{cp}\cos(\frac{\pi}{3} + \varphi_{Lcp} - \beta)} \tag{13}$$

The overall parallel misalignment amount along the Z and Y directions is obtained by combining the misalignment of bolt holes A, B and C at the side of shaft 1.

$$\begin{aligned} \eta_{pz} &= (OA' - R_c)\cos\varphi_{Lcp} + (R_c - OB')\cos\left(\varphi_{Lcp} + \tfrac{2\pi}{3}\right) + (R_{cp} - OC')\cos\left(\varphi_{Lcp} + \tfrac{4\pi}{3}\right) \\ \eta_{py} &= (OA' - R_c)\sin\varphi_{Lcp} + (R_c - OB')\sin\left(\varphi_{Lcp} + \tfrac{2\pi}{3}\right) + (R_{cp} - OC')\sin\left(\varphi_{Lcp} + \tfrac{4\pi}{3}\right) \end{aligned} \tag{14}$$

Because the parallel misalignment is small, it is considered that there is a linear relationship between the misalignment force and the misalignment,

$$\begin{aligned} F_{py} &= K_p\eta_{py} \\ F_{pz} &= K_p\eta_{pz} \end{aligned} \tag{15}$$

where K_p is the radial stiffness of the flexible coupling.

When solving the angular misalignment, the misalignment angle is projected to the $0YX$ plane. ϑ_{Zst} is the static misalignment angle around Z, and ϑ_{Zcp} is the dynamic misalignment angle, i.e., the angle difference between the two shafts at the coupling, $\vartheta_{Zcp} = \vartheta_{Z1}(L_{cp1}, t) - \vartheta_{Z2}(L_{cp2}, t)$. The total angular misalignment is the sum of both, $\vartheta_Z = \vartheta_{Zst} + \vartheta_{Zcp}$. $A'A$ is the stretched length of the diaphragm, and it changes with the rotation of the shaft. When $\angle AOA' = \vartheta_Z$, the longest length is obtained according to the cosine theorem,

$$AA'_{\max} = R_{cp}\sqrt{2 - 2\cos\vartheta_z} \tag{16}$$

Hence, the angular misalignment is yielded by

$$AA' = R_{cp}\sin\varphi_{Lcp}\sqrt{2 - 2\cos\vartheta_z} \tag{17}$$

Similarly, the misalignments of bolts B and C are acquired,

$$\begin{aligned} BB_1 &= R_c \sin(\varphi_{Lcp} + \tfrac{2\pi}{3})\sqrt{2 - 2\cos\vartheta_z} \\ CC_1 &= R_c \sin(\varphi_{Lcp} + \tfrac{4\pi}{3})\sqrt{2 - 2\cos\vartheta_z} \end{aligned} \quad (18)$$

In practice, the angular deviation is small, and the relationship between the misalignment force, deformation and distance is assumed to be linear,

$$F_A = K_a AA', F_B = K_a BB', F_C = K_a CC' \quad (19)$$

where K_a is the angular stiffness of the flexible coupling. These forces are decomposed in the radial direction to obtain

$$F_{ZAR} = D_Z \sin\varphi_{Lcp} \sin\vartheta_Z, F_{ZBR} = D_Z \sin(\varphi_{Lcp} + \frac{2\pi}{3}) \sin\vartheta_Z, F_{ZCR} = D_Z \sin(\varphi_{Lcp} + \frac{4\pi}{3}) \sin\vartheta_Z \quad (20)$$

where $D_Z = k_a R_{cp}\sqrt{2 - 2\cos\vartheta_Z}$. Similarly, the angular misalignment around Y is projected to the $0ZX$ plane, and $\vartheta_Y = \vartheta_{Yst} + \vartheta_{Ycp}$. ϑ_{Yst} and ϑ_{Ycp} are the static misalignment and dynamic misalignment angle, respectively. Similarly, $D_Y = K_a R_{cp}\sqrt{2 - 2\cos\theta_Y}$ is assumed, and one obtains

$$F_{YAR} = D_Y \cos\varphi_{Lcp} \sin\vartheta_Y, F_{YBR} = D_Y \cos(\varphi_{Lcp} + \frac{2\pi}{3}) \sin\vartheta_Y, F_{YCR} = D_Y \cos(\varphi_{Lcp} + \frac{4\pi}{3}) \sin\vartheta_Y \quad (21)$$

where the radial force can be decomposed in the Y and Z directions for F_{ZAR}

$$F_{ZAZ} = \left|D_Z \sin(]\varphi_{Lcp}) \sin(\vartheta_Z)\right| \cos(\varphi_{Lcp} + \pi), F_{ZAY} = \left|D_Z \sin(\varphi_{Lcp}) \sin(\vartheta_Z)\right| \sin(\varphi_{Lcp} + \pi) \quad (22)$$

Similarly, $F_{ZBR}, F_{ZCR}, F_{YAR}, F_{YBR}, F_{YCR}$ are decomposed in the Y and Z directions. Combined forces are obtained after summing the forces at bolts A, B and C

$$\begin{aligned}
&F_{ZZ} = F_{ZAZ} + F_{ZBZ} + F_{ZCZ} = |D_Z \sin(\varphi) \sin(\vartheta_Z)| \cos(\varphi_{Lcp} + \pi) \\
&+\left|D_Z \sin(\varphi_{Lcp} + \tfrac{2\pi}{3}) \sin(\vartheta_Z)\right| \cos(\varphi_{Lc} + \pi + \tfrac{2\pi}{3}) + \left|D_Z \sin(\varphi_{Lcp} + \tfrac{4\pi}{3}) \sin(\vartheta_Z)\right| \cos(\varphi_{Lcp} + \pi + \tfrac{4\pi}{3}) \\
&F_{ZY} = F_{ZAY} + F_{ZBY} + F_{ZCY} = |D_Z \sin(\varphi) \sin(\vartheta_Z)| \sin(\varphi_{Lcp} + \pi) \\
&+\left|D_Z \sin(\varphi_{Lcp} + \tfrac{2\pi}{3}) \sin(\vartheta_Z)\right| \sin(\varphi_{Lc} + \pi + \tfrac{2\pi}{3}) + \left|D_Z \sin(\varphi_{Lcp} + \tfrac{4\pi}{3}) \sin(\vartheta_Z)\right| \sin(\varphi_{Lcp} + \pi + \tfrac{4\pi}{3}) \\
&F_{YZ} = F_{YAZ} + F_{YBZ} + F_{YCZ} = |D_Y \cos(\varphi) \sin(\vartheta_Y)| \cos(\varphi_{Lcp} + \pi) \\
&+\left|D_Y \cos(\varphi_{Lcp} + \tfrac{2\pi}{3}) \sin(\vartheta_Y)\right| \cos(\varphi_{Lc} + \pi + \tfrac{2\pi}{3}) + \left|D_Y \cos(\varphi_{Lcp} + \tfrac{4\pi}{3}) \sin(\vartheta_Y)\right| \cos(\varphi_{Lcp} + \pi + \tfrac{4\pi}{3}) \\
&F_{YY} = F_{YAY} + F_{YBY} + F_{YCY} = |D_Y \cos(\varphi) \sin(\vartheta_Y)| \sin(\varphi_{Lcp} + \pi) \\
&+\left|D_Y \cos(\varphi + \tfrac{2\pi}{3}) \sin(\vartheta_Y)\right| \sin(\varphi_{Lcp} + \pi + \tfrac{2\pi}{3}) + \left|D_Y \cos(\varphi_{Lcp} + \tfrac{4\pi}{3}) \sin(\vartheta_Y)\right| \sin(\varphi_{Lcp} + \pi + \tfrac{4\pi}{3})
\end{aligned} \quad (23)$$

3. Vibration Suppression of the Dry Friction Damper and Equations of Motion

The damping ring allows the shaft to pass through and has radial clearance with the sleeve on the shaft. A cover plate is placed on it to confine the slide of the ring and transmit the transverse force from the spring, as shown in Figure 1. Reasonable assumptions are made as follows: the effect of the damper on the model of the shaft can be simplified as the concentrated force. The magnitude and direction of the forces from the plate on two bushings are the same. The torque around the X-axis from the tangential friction between the sleeve and the ring is not enough to rotate the ring. All sliding friction conforms to Coulomb's law.

3.1. Multiple Stages

When the speed approaches resonance, the sleeve starts bouncing inside the damping hole. For illustrative purposes, the vibration displacement of the shaft is assumed to be upward, with the motion driving the sleeve to contact the inner surface of the damping hole when the amplitude is greater than the gap. Then, the dry friction damper starts to work. Cutting the damper along the datum of Figure 1, the vibration suppression process is divided into three stages, as shown in Figure 5. The subscripts I, II and III are used to represent the 1st, 2nd, and 3rd stage.

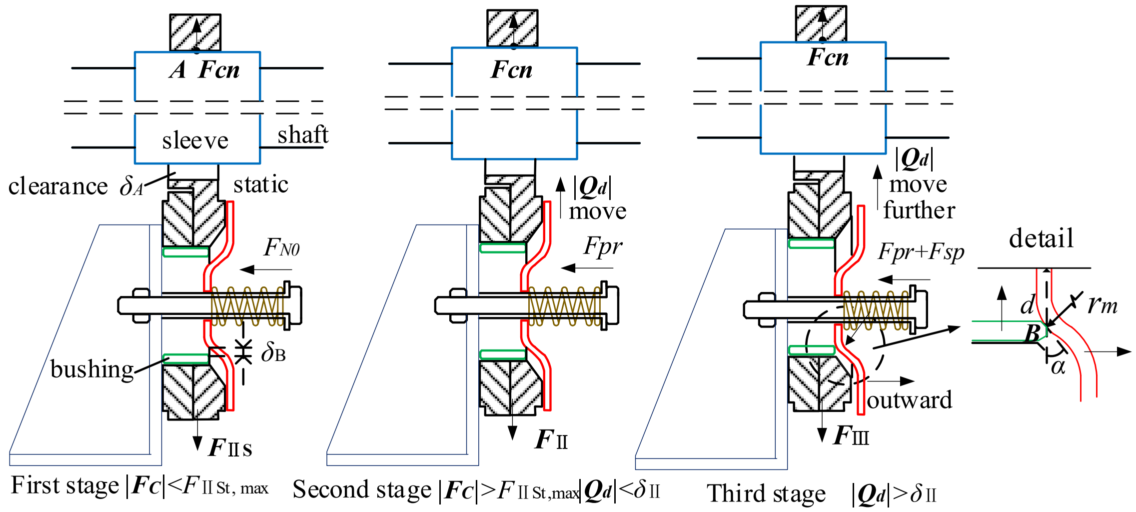

Figure 5. Three damping stages of the damper (the diameters of the shaft and sleeve are exaggeratedly reduced). Detail: The chamfer on the bushing is in contact with the fillet on the plate.

The first stage: The pre-tightening force F_{N0} of the spring is put on the plate to press the ring on the base, bringing about downward static friction $\boldsymbol{F}_{\text{IIst}}$, which resists the upward rub-impact force from the sleeve. The ring cannot move since the rub-impact force is less than the maximum static friction $F_{\text{II}st,\max}$.

The second stage: The ring begins to move once the rub-impact force exceeds $F_{\text{II}st,\max}$, which drives the bushing to move before the chamfer on the sleeve contacts the fillet on the plate, i.e., $|\boldsymbol{Q}_d| = \delta_A$. The ring is subject to sliding friction $\boldsymbol{F}_{\text{II}}$ in this stage.

The third stage: The sleeve continues to move upwards with the ring, and the bushing moves upwards against the fillet on the plate, which forces the plate outward and compresses the springs to increase the spring force on the plate. The ring is no longer subjected to sliding friction but the limiting force $\boldsymbol{F}_{\text{III}}$ from the plate. See the Appendix A for more details.

In addition to these three stages, there are also some transition stages.

3.2. Dual Rub-Impact Model

The mutual motion between the sleeve in shaft 1 and the ring in damper 1 is shown in Figure 6. To simplify, we define $\boldsymbol{Q}_s = v(L_{d1}, t) + w(L_{d1}, t), \boldsymbol{O}_d = v_{d1} + w_{d1}$ for the amplitude vector of the sleeve and ring. O, O_e, O_h, O_d are the origin of the coordinates, the eccentricity of the shaft at this point, the centroid of the sleeve after vibration, and the centroid of the ring, respectively. O_g, O_b are the centroid of the plate and bushing. In the first stage, the normal impact force is in the direction of $\boldsymbol{Q}_s$. The rub impact between the sleeve and the ring is similar to the traditional rotor-stator (static), as presented on the left in Figure 6. O_g coincides with O_b.

In the second and third stages, the ring is no longer static but moves from O to O_d, which brings about an increase in the DOFs of the system. The normal impact force is no longer in the direction of $\boldsymbol{Q}_s$ but in the direction of the vector difference between the sleeve and the ring, i.e., $\boldsymbol{O}_j = \boldsymbol{O}_s - \boldsymbol{O}_d$. The rub impact becomes a situation in which both the shaft and the ring are moving. The bushing centre O_g is moving to O_b, forming a vector $\boldsymbol{Q}_g$.

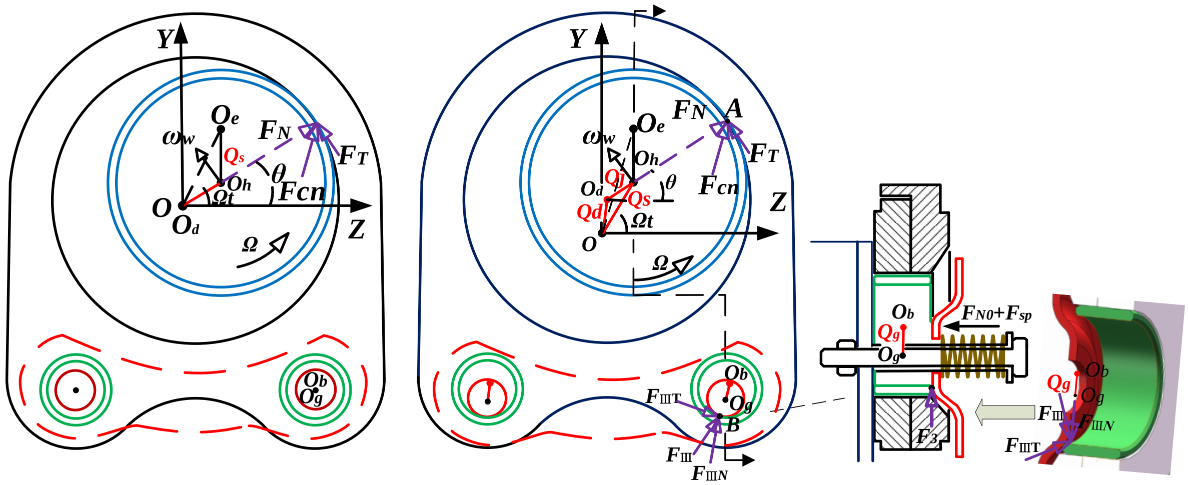

Figure 6. Rub impact between the sleeve and damper ring, (**left**) the first stage, (**right**) the third stage. Detail: The chamfer on the sleeve impacts the fillet on the plate.

3.2.1. The First Rub-Impact with Variable DOFs

The first rub-impact refers to mutual motion between the ring and sleeve, which are subject to the same magnitude of rub-impact force but in the opposite direction. Furthermore, the displacement of the shaft should be the superposition of each mode, while the ring does not require this procedure since it is a single DOF. The magnitudes of the normal impact force and tangential friction force are obtained by:

$$
\begin{aligned}
&|\boldsymbol{F}_N| = \begin{cases} K_{cn}(|\boldsymbol{Q}_s| - \delta_A) & |\boldsymbol{F}_N| - F_{\mathrm{IISmax}} \geq 0(1\mathrm{st}) \\ K_{cn}(|\boldsymbol{O}_j| - \delta_A) & |\boldsymbol{F}_N| - F_{\mathrm{IISmax}} < 0(2\mathrm{nd\ or\ }3\mathrm{rd}) \end{cases} \\
&|\boldsymbol{F}_T| = u_{dh}|\boldsymbol{F}_N| \\
&\boldsymbol{Q}_s = Q_{sz} + \mathrm{i}Q_{sy} = \sum_{r=1}^{+\infty} \Phi_r(x) Q_{v,r}(t)\Big|_{x=Lh} + \mathrm{i}\sum_{r=1}^{+\infty} \Phi_r(x) Q_{w,r}(t)|_{x=Lh} \\
&\boldsymbol{Q}_d = Q_{dv} + \mathrm{i}Q_{dw} \\
&1\mathrm{st}\ :\ |\boldsymbol{F}_c| - F_{\mathrm{IISmax}} \geq 0 \\
&2\mathrm{nd\ or\ }3\mathrm{rd}\ :\ |\boldsymbol{F}_c| - F_{\mathrm{IISmax}} < 0
\end{aligned}
\tag{24}
$$

where δ_A is the clearance between the sleeve and ring. The forces at each stage can be unified as

$$
\begin{aligned}
\boldsymbol{F}_{cn} &= \boldsymbol{F}_N + \boldsymbol{F}_T = \Theta_{\mathrm{I}} K_{cn}(1 + \mathrm{i}\mu_{dh}\mathrm{sgn}(v_{cn}))\left(\boldsymbol{O}_j - \delta_A \frac{\boldsymbol{O}_j}{|\boldsymbol{Q}_s - \boldsymbol{Q}_d|}\right) \\
v_{cn} &= |\boldsymbol{O}_j|\omega_w + \Omega R_h
\end{aligned}
\tag{25}
$$

where Θ_{I} is the Heaviside condition. v_{cn} is the velocity of the sleeve at the contact point of the damping ring. If the whirl direction of ω_w is the same as the spin of the shaft, it is a forward whirl; otherwise, it is a reverse whirl. Unlike the rotor-stator system, the rub-impact force in this work cannot be directly applied to the right-hand side of the shaft vibration equation; instead, it should be converted into the generalized force of each mode, which is expressed as

$$
\boldsymbol{F}_{cn,r} = \int_0^L \boldsymbol{F}_{cn}\gamma(x - L_h)\Phi_r(x)dx \tag{26}
$$

3.2.2. Radical Impact Stiffness of the First Rub Impact

The radical impact stiffness in the rub-impact model is an important criterion for determining the accuracy of the mathematical simulation. The stiffness of the ring made from the polymerization of graphite, POB (Polybenzoate) and PTFE (Polytetrafluoroethylene) is quite different from that of the metal stator and needs to be studied in depth.

1. Linearization of the local surface stiffness

The contact and deformation of the object surface are complicated nonlinear behaviors. In light of ref. [22], using the equivalent linear spring force model with an appropriate stiffness can simulate the effect of the nonlinear extrusion process. Thus, the stiffness resisting impaction in the surface of the damping ring is like having springs on its surface, where the linearized equivalent stiffness is treated as

$$K_{ex} = \xi\left(\frac{M_d}{M_r + M_d}\frac{T_0}{\varsigma^6}\right)^{1/5} \tag{27}$$

where M_r, M_d are the mass of the collider, i.e., the mass of the shaft and ring. $T_0 = M_r v_0^2/2$ is the initial kinetic energy of M_r. v_0 is the velocity difference between the sleeve and the ring before every impact, which fully illustrates that this stiffness changes with v_0. ξ is the conversion coefficient, $\xi \approx 1.0948$. ς is related to the surface shape of two objects; in case of an outer circle contacts the inner circle,

$$\varsigma = 0.8\sqrt[3]{\frac{9}{16}\left(\frac{1-v_h^2}{E_h} + \frac{1-v_d^2}{E_d}\right)^2\left(\frac{1}{R_h} - \frac{1}{R_d}\right)} \tag{28}$$

where E_h E_d v_h v_d R_h R_d are the elastic modulus, Poisson's ratio and radius of the sleeve and damping hole, respectively.

2. Impact stiffness of the damping ring

For the damping ring in this work, only considering the local surface elastic deformation at the collision position and ignoring other positions of the ring is inconsistent with the practical situation. The elasticity of the damping ring should also be investigated since its deformation can also resist impact. This is the maximal difference between this work and the traditional metal stator. The FEA method is adopted to analyze the elastic deformation of the ring after impact. The force is applied on different points around the hole from the sleeve. The deformation of the damping ring when the collision point is at the top is displayed in Figure 7. The stiffness is acquired by dividing the force by the displacement distance of the internal node away from the surface.

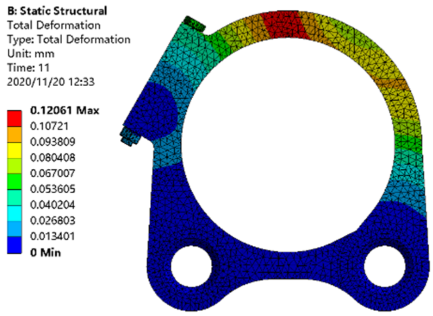

Figure 7. The deformation of the dry friction damper when the collision point is at the top of the damping ring obtained by the FEA method.

The FEA results show that the anti-deformation stiffness on the top of the ring is larger than that on the bottom, for which the structure and supporting hole location of the ring can be determined. The ring is divided into four parts, and the relationship of the stiffness $K_{de\theta}$ for each part based on the top part K_{de} with the collision angle θ is shown in Table 1.

Table 1. Anti-deformation stiffness with collision angle θ.

θ	0	90	180	270
$K_{de\theta}$	1.9	1	1.95	4.6

The coeffect of the anti-deformation stiffness and local surface stiffness has been assumed to be independent of each other and similar to the series connection of two springs. Therefore, the impact stiffness in the rub impact model can be approximately treated as

$$K_{cn}(\theta) = \frac{K_{de\theta}K_{ex}}{K_{de\theta} + K_{ex}} \tag{29}$$

We found that the local surface stiffness is one order of magnitude larger than the anti-deformation stiffness; hence, the anti-deformation stiffness is at the dominant position in the form of Equation (29). $K_{de\theta}$ can even denote K_{cn} after ignoring the existence of K_{ex} for engineering use, which is consistent with ref. [18], where only flexible deformation of a cylindrical shell rotor is employed in the impact stiffness.

3.2.3. The Second Rub-Impact with Nonlinear Restricted Stiffness

If the norm of $\boldsymbol{Q_g}$ is more than the vertical distance between the chamfer on the bushing and the fillet on the plate, i.e., $\left|\boldsymbol{Q_g}\right| > \delta_B$, it enters the third stage, as shown in Figures 5 and 6. The second rub impact occurs between bushing and plate at point A, and the red circle is centred at O_g with a radius of length from A to O_g.

$$\boldsymbol{F}_{\mathrm{III}} = \boldsymbol{F}_{\mathrm{III,N}} + \boldsymbol{F}_{\mathrm{III,T}} = K_{\mathrm{III}}(1 + \mathrm{i}\mu_3)(1 - \frac{\delta_{\mathrm{II}}}{\left|\boldsymbol{Q_g}\right|})\boldsymbol{Q_g} \tag{30}$$

Given the previous assumption, the ring cannot rotate so $\boldsymbol{F}_{\mathrm{IIIT}} \approx 0$ and $\boldsymbol{F}_{\mathrm{IIIN}} \approx \boldsymbol{F}_{\mathrm{IIIT}}$, and $\boldsymbol{F}_{\mathrm{III}}$ is related to the motion displacement of the ring. Since the bushing is moving with the ring, $\boldsymbol{Q_g} = \boldsymbol{Q_d}$. K_{III} is the restricted stiffness derived from the restriction relationship of each component in the dry friction damper, as shown in the Appendix A.

$$K_{\mathrm{III}} = \frac{2\left[F_{N0} + K_{sp}(|\boldsymbol{Q_d}| - \delta_B)\tan\alpha\right]\left[(\mu_3 + \mu_4)\cos\alpha + (1 - \mu_4\mu_3)\sin\alpha\right]}{(|\boldsymbol{Q_d}| - \delta_B)\left[(1 - \mu_5\mu_3)\cos\alpha - (\mu_3 + \mu_5)\sin\alpha\right]} \tag{31}$$

It is obvious that the stiffness which relates to the parameters of the system is nonlinear and varies with angle α and vibration displacement $\boldsymbol{Q_d}$.

In summary, the innovative contributions of this section are described as: A novel dual rub-impact model between the shaft and dry friction damper with multiple stages is proposed. The first rub-impact characterized by variable DOFs and coupled impact stiffness, as well as the second rub-impact with nonlinear stiffness are addressed.

3.3. Equations of Motion

In addition to the above forces, when the ring is impacted by the sleeve in the 1st stage, the rub impact force is resisted by the static friction force,

$$F_{\mathrm{IISmax}} = F_{pr}(\mu_1 + \mu_2) \tag{32}$$

where μ_1, μ_2 are static friction coefficients between the ring and plate and the ring and the base, respectively. In the 2nd stage, the sliding friction force on the ring is opposite to its moving direction and slightly less than the maximum static friction,

$$\boldsymbol{F}_{\mathrm{II}} = \frac{\varepsilon F_{\mathrm{IISmax}}\boldsymbol{Q_d}}{|\boldsymbol{Q_d}|} \tag{33}$$

To obtain the equations of motion, separated variables are constructed as follows:

$$\begin{aligned}&\boldsymbol{Q_{s1}}(x,t)=\boldsymbol{\Phi_1}(x)\mathbf{Q}(t),\boldsymbol{Q_{s2}}(x,t)=\boldsymbol{\Phi}_2(x)\mathbf{Q}(t),\\&\phi_1(x,t)=\boldsymbol{\Phi}_{\phi1}(x)\mathbf{Q}(t),\phi_2(x,t)=\boldsymbol{\Phi}_{\phi2}(x)\mathbf{Q}(t),\\&e_1(x)=\boldsymbol{\Phi_1}(x)e_{r1},e_2(x)=\boldsymbol{\Phi}_2(x)e_{r2}\end{aligned}\tag{34}$$

where $\boldsymbol{Q_{s1}}(x,t)=v_1(x,t)+\mathrm{i}w_1(x,t)$ and $\boldsymbol{Q_{s2}}(x,t)=v_2(x,t)+\mathrm{i}w_2(x,t)$. The row vectors of the modal function that satisfy the boundary conditions are as follows,

$$\begin{aligned}
\boldsymbol{\Phi_1}(x)&=\left[\begin{matrix}\underbrace{\sin\frac{\pi x}{L_1}\quad\sin\frac{2\pi x}{L_1}\quad\cdots\quad\sin\frac{r\pi x}{L_1}}_{r}\quad\underbrace{0\quad0\quad0\quad\cdots\quad0}_{r}\quad0\quad0\end{matrix}\right]\\
\boldsymbol{\Phi_2}(x)&=\left[\begin{matrix}\underbrace{0\quad0\quad\cdots\quad0}_{r}\quad0\quad\underbrace{\sin\frac{\pi(x-L_1)}{L_2}\quad\sin\frac{2\pi(x-L_1)}{L_2}\quad\cdots\quad\sin\frac{r\pi(x-L_1)}{L_2}}_{r}\quad0\quad0\end{matrix}\right]\\
\boldsymbol{\Phi_{d1}}(x)&=\left[\begin{matrix}\underbrace{0\quad0\quad\cdots\quad0}_{r}\quad1\quad\underbrace{0\quad0\quad\cdots\quad0}_{r}\quad0\quad0\end{matrix}\right]\\
\boldsymbol{\Phi_{d2}}(x)&=\left[\begin{matrix}\underbrace{0\quad0\quad\cdots\quad0}_{r}\quad0\quad\underbrace{0\quad0\quad\cdots\quad0}_{r}\quad1\quad0\end{matrix}\right]\\
\boldsymbol{\Phi}_{\phi1}(x)&=\left[\begin{matrix}\underbrace{0\quad0\quad\cdots\quad0}_{r}\quad0\quad\underbrace{0\quad0\quad\cdots\quad0}_{r}\quad0\quad\frac{x}{L_1}\end{matrix}\right]\\
\boldsymbol{\Phi}_{\phi2}(x)&=\left[\begin{matrix}\underbrace{0\quad0\quad\cdots\quad0}_{r}\quad0\quad\underbrace{0\quad0\quad\cdots\quad0}_{r}\quad0\quad\frac{x}{L_2}\end{matrix}\right]
\end{aligned}\tag{35}$$

where r is the number of modes. As with all vibrating systems, when the equilibrium position is taken as the initial position, gravity can be removed from the right side of the equation. The system dynamic equation is obtained via the Lagrange equation,

$$\frac{d}{dt}\left(\frac{\partial T}{\partial Q}\right)-\frac{\partial T}{\partial Q}+\frac{\partial U}{\partial Q}+\frac{\partial V}{\partial Q}=F\tag{36}$$

The equation of motion of the helicopter tail rotor driveline system can be obtained by combining the rub impact forces of the three stages and Equation (35), then the equation of motion can be written in matrix form as follows

$$\mathbf{M}\ddot{\mathbf{Q}}+(\mathbf{C_n}+\mathbf{C_{ct}}+\Omega\mathrm{i}\mathbf{G})\dot{\mathbf{Q}}+(\mathbf{K}-\Omega\mathrm{i}\mathbf{K_{ct}})\mathbf{Q}=\mathbf{m_e}\Omega^2e^{\mathrm{i}\Omega t}-\mathbf{F_{cn}}+\mathbf{F}_{\mathrm{III}}+\mathbf{F}_{\mathrm{II}}+\mathbf{F_P}+\mathbf{F_a}+\mathbf{N}\tag{37}$$

where

$$\begin{aligned}
&\mathbf{M}=\mathbf{M_S}+\mathbf{M_D}\\
&\mathbf{M_S}=\int_0^{L_1}\left(\rho_1A_1\boldsymbol{\Phi_1}^T\boldsymbol{\Phi_1}+\rho_1I_1\boldsymbol{\Phi'_1}^T\boldsymbol{\Phi'_1}+2\rho_1I_1\boldsymbol{\Phi'}_{\phi1}{}^T\boldsymbol{\Phi'}_{\phi1}\right)dx+\int_0^{L_2}\left(\rho_2A_2\boldsymbol{\Phi_2}^T\boldsymbol{\Phi_2}+\rho_2I_2\boldsymbol{\Phi'_2}^T\boldsymbol{\Phi'_2}+2\rho_2I_2\boldsymbol{\Phi'}_{\phi2}{}^T\boldsymbol{\Phi'}_{\phi2}\right)dx\\
&+\sum_{i=1}^{su1}\left[m_{h1,i}\boldsymbol{\Phi_1}^T\boldsymbol{\Phi_1}\big|_{x=L_{h1,i}}+\rho_{h1}I_{hz1,i}\boldsymbol{\Phi'_1}^T\boldsymbol{\Phi'_1}\Big|_{x=L_{h1,i}}\right]+\sum_{i=1}^{su2}\left[m_{h2,i}\boldsymbol{\Phi_2}^T\boldsymbol{\Phi_2}\big|_{x=L_{h2,i}}+\rho_{h2}I_{hz2,i}\boldsymbol{\Phi'_2}^T\boldsymbol{\Phi'_2}\Big|_{x=L_{h2,i}}\right]+J_L\boldsymbol{\Phi'_2}^T\boldsymbol{\Phi'_2}\Big|_{x=L_2}\\
&\mathbf{M_D}=\Theta_{1,2}m_{d1}\boldsymbol{\Phi_{d1}}^T\boldsymbol{\Phi_{d1}}+\Theta_{2,2}m_{d2}\boldsymbol{\Phi_{d2}}^T\boldsymbol{\Phi_{d2}}\\
&\mathbf{G}=2\rho_1I_1\int_0^{L_1}\boldsymbol{\Phi'_1}^T\boldsymbol{\Phi'_1}dx+\sum_{i=1}^{n1}\left[2\rho_{h1}I_{hz1,i}\boldsymbol{\Phi'_1}^T\boldsymbol{\Phi'_1}\Big|_{x=L_{h1,i}}\right]+2\rho_2I_2\int_0^{L_2}\boldsymbol{\Phi'_2}^T\boldsymbol{\Phi'_2}dx+\sum_{i=1}^{n1}\left[2\rho_{h2}I_{hz2,i}\boldsymbol{\Phi'_2}^T\boldsymbol{\Phi'_2}\Big|_{x=L_{h2,i}}\right]\\
&\mathbf{K}=\int_0^{L_1}\left(E_1I_1\boldsymbol{\Phi''}_1{}^T\boldsymbol{\Phi''}_1+2G_{\phi1}I_1\boldsymbol{\Phi'}_{\phi1}{}^T\boldsymbol{\Phi'}_{\phi1}\right)dx+k_{n1}\boldsymbol{\Phi_1}^T\boldsymbol{\Phi_1}\big|_{x=L_{n1}}+E_2I_2\int_{L_1}^{L_2}\left(\boldsymbol{\Phi''_2}^T\boldsymbol{\Phi''_2}+2G_{\phi2}I_2\boldsymbol{\Phi'}_{\phi2}{}^T\boldsymbol{\Phi'}_{\phi2}\right)dx+k_{n2}\boldsymbol{\Phi_2}^T\boldsymbol{\Phi_2}\big|_{x=L_{n2}}\\
&\mathbf{m_e}=\int_0^{L_1}e_{r1}\rho A\boldsymbol{\Phi_1}^T\boldsymbol{\Phi_1}dx+\sum_{i=1}^{n}\left[m_{eh,i}e_{h,i}\boldsymbol{\Phi_1}^T\boldsymbol{\Phi_1}\big|_{x=L_{h1,i}}\right]+\int_0^{L_2}e_{r2}\rho A\boldsymbol{\Phi_2}^T\boldsymbol{\Phi_2}dx+\sum_{i=1}^{n}\left[m_{eh,i}e_{h,i}\boldsymbol{\Phi_2}^T\boldsymbol{\Phi_2}\big|_{x=L_{h2,i}}\right]\\
&\mathbf{K_{rt}}=\int_0^{L_1}(E_1I_1\boldsymbol{\Phi''}_1{}^T\boldsymbol{\Phi''}_1)dx+K_{n1}\boldsymbol{\Phi_1}^T\boldsymbol{\Phi_1}\big|_{x=L_{n1}}+E_2I_2\int_{L_1}^{L_2}(\boldsymbol{\Phi''_2}^T\boldsymbol{\Phi''_2})dx+K_{n2}\boldsymbol{\Phi_2}^T\boldsymbol{\Phi_2}\big|_{x=L_{n2}}\\
&\mathbf{C_{rt}}=c_{vi}\mathbf{K}\\
&\mathbf{C_n}=\mathbf{C_{ns}}+\mathbf{C_{rt}}\\
&\mathbf{C_{ns}}=c_{n1}\boldsymbol{\Phi_1}^T\boldsymbol{\Phi_1}\big|_{x=L_{n1}}+c_{n2}\boldsymbol{\Phi_2}^T\boldsymbol{\Phi_2}\big|_{x=L_{n2}}\\
&\mathbf{C_{nd}}=\Theta_{1,\mathrm{II}}c_{d1}\boldsymbol{\Phi_{d1}}^{\mathbf{T}}\boldsymbol{\Phi_{d1}}+\Theta_{2,\mathrm{II}}c_{d2}\boldsymbol{\Phi_{d2}}^{\mathbf{T}}\boldsymbol{\Phi_{d2}}
\end{aligned}\tag{38}$$

Considering that there is more than one sleeve, disc, and damper on one shaft in this or other systems, the subscript i represents the i-th sleeve, disc, or damper. $\mathbf{M},\mathbf{C_n},\mathbf{C_{rt}},\mathbf{G},\mathbf{K},\mathbf{K_{rt}}$

denote the matrix composed of each mode of mass, nonrotating external damping, rotating viscous internal damping, gyroscopic moment, stiffness, and additional stiffness due to viscous internal damping in the rotating coordinate system, respectively. $\mathbf{M_d}, \mathbf{C_d}$ are the matrix of the mass of the ring and energy dissipation in the slide of the ring in the 2nd and 3rd stages. $\mathbf{F_{cn}}, \mathbf{F}_{\mathrm{II}}, \mathbf{F}_{\mathrm{III}}, \mathbf{F_p}, \mathbf{F_a}, \mathbf{m_e}$ denote the matrix composed of each mode of the force in rub impact, the force in the 2nd stage, the force in the 3rd stage, the force caused by parallel misalignment, angular misalignment, and the force caused by eccentricity, respectively,

$$\begin{aligned}
&\mathbf{F_{cn}} = \Theta_{1,\mathrm{I}}\boldsymbol{F_{cn1}}(\boldsymbol{\Phi}_1^{\mathbf{T}} - \Theta_{1,\mathrm{II}}\boldsymbol{\Phi}_{\mathbf{d1}}^{\mathbf{T}}) + \Theta_{2,\mathrm{I}}\boldsymbol{F_{cn2}}(\boldsymbol{\Phi}_2^{\mathbf{T}} - \Theta_{2,\mathrm{II}}\boldsymbol{\Phi}_{d2}^{\mathbf{T}}) \\
&\mathbf{F}_{\mathrm{II}} = \Theta_{1,\mathrm{II}}(1-\Theta_{1,\mathrm{III}})\boldsymbol{F}_{1,\mathrm{II}} + \Theta_{2,\mathrm{II}}(1-\Theta_{2,\mathrm{III}})\boldsymbol{F}_{\mathbf{2},\mathrm{II}} \\
&\mathbf{F}_{\mathrm{III}} = \Theta_{1,\mathrm{II}}\Theta_{1,\mathrm{III}}\boldsymbol{F}_{1,\mathrm{III}} + \Theta_{2,\mathrm{II}}\Theta_{2,\mathrm{III}}\boldsymbol{F}_{\mathbf{2},\mathrm{III}} \\
&\mathbf{F_p} = F_p\boldsymbol{\Phi}_{\mathbf{1c}}^{\mathbf{T}} - F_p\boldsymbol{\Phi}_{\mathbf{2c}}^{\mathbf{T}} \\
&\mathbf{F_a} = F_a\boldsymbol{\Phi}_{\mathbf{1c}}^{\mathbf{T}} - F_a\boldsymbol{\Phi}_{\mathbf{2c}}^{\mathbf{T}} \\
&\mathbf{N} = N\boldsymbol{\Phi}^{\mathbf{T}}{}_{\mathbf{1s}}
\end{aligned} \tag{39}$$

To distinguish, the Roman numerals representing the damping stage are placed in the second place of the subscript. For convenience, we define

$$\boldsymbol{\Phi}_{\mathbf{c}2}^{\mathbf{T}} = \boldsymbol{\Phi}_{\mathbf{2}}^{\mathbf{T}}\Big|_{\mathbf{x}=Lcp2}, \ \boldsymbol{\Phi}_{\mathbf{c}1}^{\mathbf{T}} = \boldsymbol{\Phi}_{\mathbf{1}}^{\mathbf{T}}\Big|_{\mathbf{x}=Lcp1}, \boldsymbol{\Phi}_{h1}^{\mathbf{T}} = \boldsymbol{\Phi}_{\mathbf{1}}^{\mathbf{T}}\Big|_{\mathbf{x}=Lh1}, \boldsymbol{\Phi}_{h2}^{\mathbf{T}} = \boldsymbol{\Phi}_{\mathbf{2}}^{\mathbf{T}}\Big|_{\mathbf{x}=Lh2}, \boldsymbol{\Phi}^{\mathbf{T}}{}_{\mathbf{1s}} = \boldsymbol{\Phi}_{\mathbf{2}}^{\mathbf{T}}\Big|_{\mathbf{x}=0} \tag{40}$$

$\Theta_{1,\mathrm{I}}, \Theta_{1,\mathrm{II}}, \Theta_{1,\mathrm{III}}$ and $\Theta_{2,\mathrm{I}}\Theta_{2,\mathrm{II}}, \Theta_{2,\mathrm{III}}$ are the Heaviside conditions for the 1st, 2nd and 3rd stage of shaft 1 and shaft 2, respectively,

$$\begin{aligned}
&\text{shaft 1 }: \Theta_{1,\mathrm{I}} = \begin{cases} 1 & \left|(\boldsymbol{\Phi}_{h1} - \boldsymbol{\Phi}_{\mathbf{d1}})\mathbf{Q}\right| \ge \delta_{1,A} \\ 0 & \left|(\boldsymbol{\Phi}_{h1} - \boldsymbol{\Phi}_{\mathbf{d1}})\mathbf{Q}\right| < \delta_{1,A} \end{cases}, \Theta_{1,\mathrm{II}} = \begin{cases} 1 & |\boldsymbol{F}_{c1}| - F_{\mathrm{ISmax}} \ge 0 \\ 0 & |\boldsymbol{F}_{c1}| - F_{\mathrm{ISmax}} < 0 \end{cases}, \Theta_{1,\mathrm{III}} = \begin{cases} 1 & \left|\boldsymbol{\Phi}_{\mathbf{d1}}\mathbf{Q}\right| - \delta_{1,B} \ge 0 \\ 0 & \left|\boldsymbol{\Phi}_{\mathbf{d1}}\mathbf{Q}\right| - \delta_{1,B} < 0 \end{cases} \\
&\text{shaft 2 }: \Theta_{2,\mathrm{I}} = \begin{cases} 1 & \left|(\boldsymbol{\Phi}_{h2} - \boldsymbol{\Phi}_{\mathbf{d2}})\mathbf{Q}\right| \ge \delta_{2,A} \\ 0 & \left|(\boldsymbol{\Phi}_{h2} - \boldsymbol{\Phi}_{\mathbf{d2}})\mathbf{Q}\right| < \delta_{2,A} \end{cases}, \Theta_{2,\mathrm{II}} = \begin{cases} 1 & |\boldsymbol{F}_{c2}| - F_{\mathrm{IISmax}} \ge 0 \\ 0 & |\boldsymbol{F}_{c2}| - F_{\mathrm{IISmax}} < 0 \end{cases}, \Theta_{2,\mathrm{III}} = \begin{cases} 1 & \left|\boldsymbol{\Phi}_{\mathbf{d2}}\mathbf{Q}\right| - \delta_{2,B} \ge 0 \\ 0 & \left|\boldsymbol{\Phi}_{\mathbf{d2}}\mathbf{Q}\right| - \delta_{2,B} < 0 \end{cases}
\end{aligned} \tag{41}$$

It should be noted that $\Theta_{1,\mathrm{II}}$ and $\Theta_{2,\mathrm{II}}$ determine whether the damping ring moves, that is, whether the degree of freedom of the system increases. And they are related as $\mathbf{M_d}, \mathbf{C_d}$ in Equation (38). $\mathbf{F_c}, \mathbf{F_2}, \mathbf{F_3}$ all involve four independent Heaviside conditions, but the logical relationship of the four conditions forms the condition of the existence of $\mathbf{F_c}, \mathbf{F_2}, \mathbf{F_3}$. For example, $\Theta_{1,\mathrm{II}}\Theta_{1,\mathrm{III}}$ means only if $\Theta_{1,\mathrm{II}}$ and $\Theta_{1,\mathrm{III}}$ are satisfied, $\boldsymbol{F}_{1,\mathrm{III}}$ will appear. $\Theta_{1,\mathrm{II}}\Theta_{1,\mathrm{III}}\boldsymbol{F}_{1,\mathrm{III}} + \Theta_{2,\mathrm{II}}\Theta_{2,\mathrm{III}}\boldsymbol{F}_{\mathbf{2},\mathrm{III}}$ means $\boldsymbol{F}_{1,\mathrm{III}}, \boldsymbol{F}_{\mathbf{2},\mathrm{III}}$ are independent of each other, they do not necessarily appear at the same time. These force matrices consist of the following force vectors:

$$\begin{aligned}
&\boldsymbol{F_{c1}} = K_{cn1}(\omega_{w1})(1+\mathrm{i}\mu_{dh}\mathrm{sgn}(v_{c1}))(\boldsymbol{\Phi}_{h1} - \boldsymbol{\Phi}_{\mathbf{d1}})\mathbf{Q}\left(1 - \frac{\delta_{1,A}}{\left|(\boldsymbol{\Phi}_1 - \boldsymbol{\Phi}_{\mathbf{d1}})\mathbf{Q}\right|}\right) \\
&\boldsymbol{F_{c2}} = K_{cn2}(\omega_{w2})(1+\mathrm{i}\mu_{dh}\mathrm{sgn}(v_{c2}))(\boldsymbol{\Phi}_{h2} - \boldsymbol{\Phi}_{\mathbf{d2}})\mathbf{Q}\left(1 - \frac{\delta_{2,A}}{\left|(\boldsymbol{\Phi}_2 - \boldsymbol{\Phi}_{\mathbf{d2}})\mathbf{Q}\right|}\right) \\
&v_{cn1} = \left|(\boldsymbol{\Phi}_{h1} - \boldsymbol{\Phi}_{\mathbf{d1}})\mathbf{Q}\right|\omega_{w1} + \Omega R_h, v_{cn2} = \left|(\boldsymbol{\Phi}_{h2} - \boldsymbol{\Phi}_{\mathbf{d2}})\mathbf{Q}\right|\omega_{w2} + \Omega R_h \\
&\boldsymbol{F}_{1,\mathrm{II}} = \frac{\varepsilon F_{1,\mathrm{IIstmax},}\boldsymbol{\Phi}_{\mathbf{d1}}\mathbf{Q}}{\left|\boldsymbol{\Phi}_{\mathbf{d1}}\mathbf{Q}\right|}, \boldsymbol{F}_{1,\mathrm{III}} = K_{1,\mathrm{III}}\left(1 - \frac{\delta_{1,B}}{\left|\boldsymbol{\Phi}_{\mathbf{d1}}\mathbf{Q}\right|}\right)\boldsymbol{\Phi}_{\mathbf{d1}}\mathbf{Q} \\
&\boldsymbol{F}_{2,\mathrm{II}} = \frac{\varepsilon F_{2,\mathrm{IIstmax}}\boldsymbol{\Phi}_{\mathbf{d2}}\mathbf{Q}}{\left|\boldsymbol{\Phi}_{\mathbf{d2}}\mathbf{Q}\right|}, \boldsymbol{F}_{2,\mathrm{III}} = K_{2,\mathrm{III}}\left(1 - \frac{\delta_{2,B}}{\left|\boldsymbol{\Phi}_{\mathbf{d2}}\mathbf{Q}\right|}\right)\boldsymbol{\Phi}_{\mathbf{d2}}\mathbf{Q} \\
&F_{1,\mathrm{IIstmax},} = c_f F_{pr1}(\mu_1 + \mu_2), F_{2,\mathrm{IIstmax}} = c_f F_{pr2}(\mu_1 + \mu_2)
\end{aligned} \tag{42}$$

where $F_{N0,1}, F_{N0,2}$ are the pre-tightening forces of damper 1 and damper 2. $\theta_1 = \omega_{w2}/\left|\boldsymbol{\Phi}_{h1}\mathbf{Q}\right|$ and $K_{cn1}(\omega_{w1})$ take the place of $K_{cn1}(\theta_1)$ in Equation (29).

$\mathbf{F_p}, \mathbf{F_a}$ consist of the parallel and angular misalignment force vectors,

$$\begin{aligned} &\boldsymbol{F_p} = k_p\left[(OA' - R_{cp})e^{\mathrm{i}\Omega t} + (R_{cp} - OB')e^{\mathrm{i}(\Omega t + \frac{2\pi}{3})} + (R_{cp} - OC')e^{\mathrm{i}(\Omega t + \frac{4\pi}{3})}\right] \\ &\boldsymbol{F_a} = (|D_Z \sin(\Omega t)\sin(\vartheta_z)| + |D_Y \cos(\Omega t)\sin(\vartheta_z)|)e^{\mathrm{i}(\Omega t + \pi)} + \left(\left|D_Z \sin(\Omega t + \tfrac{2\pi}{3})\sin(\vartheta_Z)\right| + \left|+D_Y \cos(\Omega t + \tfrac{2\pi}{3})\sin(\vartheta_Y)\right|\right)e^{\mathrm{i}(\Omega t + \frac{2\pi}{3} + \pi)} \\ &+\left(\left|D_Z \sin(\Omega t + \tfrac{4\pi}{3})\sin(\vartheta_Z)\right| + \left|D_Y \cos(\Omega t + \tfrac{4\pi}{3})\sin(\vartheta_Y)\right|\right)^{\mathrm{i}(\Omega t + \frac{4\pi}{3} + \pi)} \end{aligned} \tag{43}$$

Regardless of the speed fluctuation, φ_{Lcp} is replaced by Ωt. The other coefficients can be found in Section 2.2 above, where

$$\begin{aligned} &v_{cp} = \Re(\mathbf{\Phi}_{\mathbf{c1}}^{\mathbf{T}}\mathbf{Q} - \mathbf{\Phi}_{\mathbf{c2}}^{\mathbf{T}}\mathbf{Q}), w_{cp} = \Im(\mathbf{\Phi}_{\mathbf{cp1}}^{\mathbf{T}}\mathbf{Q} - \mathbf{\Phi}_{\mathbf{cp2}}^{\mathbf{T}}\mathbf{Q}) \\ &\theta_{Zcp} = -\Im(\mathbf{\Phi'}_{\mathbf{cp1}}^{\mathbf{T}}\mathbf{Q} - \mathbf{\Phi'}_{\mathbf{cp2}}^{\mathbf{T}}\mathbf{Q}), \theta_{Ycp} = \Re(\mathbf{\Phi'}_{\mathbf{cp1}}^{\mathbf{T}}\mathbf{Q} - \mathbf{\Phi'}_{\mathbf{cp2}}^{\mathbf{T}}\mathbf{Q}) \end{aligned} \tag{44}$$

where $\Re$ and $\Im$ denote the real part and the imaginary part, respectively.

The uncertainty of the model is a factor to be considered in engineering modeling. In this work, the uncertainty comes from some unexpected parameter changes, such as the looseness or abrasion of the installation part or the insensitivity region of the element, and the change of parameters with time in the operation process of the helicopter tail driveline. However, due to the frequent maintenance of the helicopter, all parts will be tested to keep them in a reasonable and safe range, and worn parts will be replaced. Therefore, this uncertainty has not attracted attention. However, it must be taken into account if this model is extended to engineering application in some harsh environments with the long-term operation.

4. Simulations and Results

The varying collision angle θ determines the impact stiffness. In the 2nd and 3rd stages, the nonlinear restricted force acting on the ring varies with the direction of vibration. Moreover, the expression of $\mathbf{F_3}$ is a varying parametric equation attributed to K_{III}; more precisely, α varies with the displacement of the ring. Therefore, Equation (37) is classified strictly as a nonconservative nonautonomous system, whose solution is usually sought by the numerical integration method, including the Euler, Runge-Kutta, and Adams-Bashforth methods.

Runge–Kutta found that the calculation speed is low for Equation (37), especially in the 3rd stage; in contrast, the method of Adams–Bashforth is faster since there are fewer mathematical calculations but with lower accuracy. The Adams–Bashforth and Runge–Kutta methods are both based on Taylor series expansion and replace the higher-order terms in the expansion with linear terms. The Adams–Bashforth method retains the expansion to the second order and replaces the second derivative with the difference. To improve accuracy, this paper uses the difference method to replace the third derivative. However, since the solution of a time step depends on the previous two steps, this method cannot start at t = 0 but starts with the Runge–Kutta method of the same order.

The implemented procedure is listed in Figure 8. It uses k to circulate and calculate the response of the double shaft. One hundred-time steps per rotational cycle are used to obtain reliable results, and the former six modes are selected for this continuous system. To guarantee that the data being used is in the steady-state, the previous two-hundred-time series data have been neglected. The results of the next hundred-time series are reserved for carrying out the analysis. The parameters are from a helicopter tail rotor driveline, as described in Table 2.

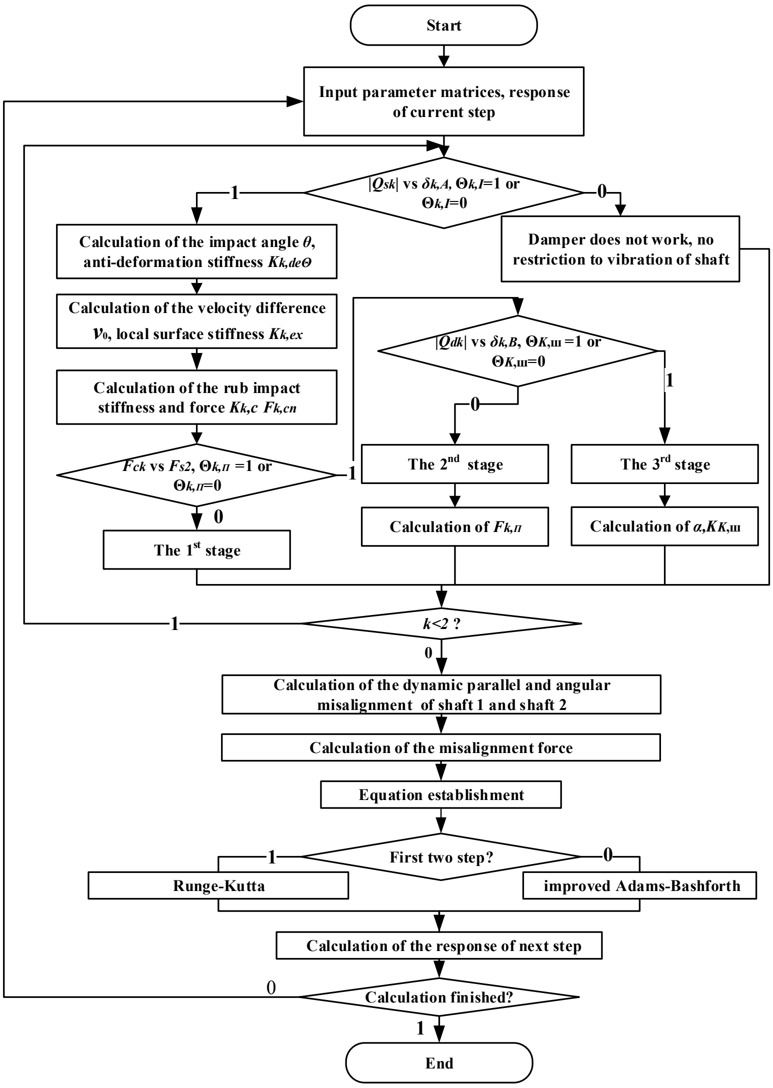

Figure 8. Computational flowchart to solve Equation (37).

Table 2. System parameters.

Parameter	Value/Unit	Parameter	Value/Unit
L_1, L_2	3653, 3514 mm	L_{s1}, L_{s2}	1965, 1757 mm
L_{c1}, L_{c2}	3642, 11 mm	L_{n1}, L_{n2}	76, 76 mm
E_1, E_2	72 GPa	A_1, A_2	747 mm^2
c_s	0.0001 N s/m	I_1, I_2	1.633×10^6 mm^4
ρ_{sh}	7850 kg/M^3	ρ_1, ρ_2	2700 kg/m^3
e_{r1}, e_{r2}	0.05%, 0.04%	a	7.47×10^{-4} m^2
$\delta_{1,1}, \delta_{1,2}$	2 mm	$\delta_{1,2}, \delta_{2,2}$	1.44 mm
C_{d1}, C_{d2}	160 N s/m	R_s	0.06705 m
K_{n1}, K_{n2}	150 kN/m	m_{d1}, m_{d2}	0.4925 kg
K_{sp}	23.17 kN/m	m_{h1}, m_{h2}	0.3033 kg
m_{eh1}, m_{eh1}	0	e_{h1}, e_{h2}	0
c_f	0.8	I_{sz1}	2.055×10^{-3} m^4 m^2
E_h	1.7×10^{11} Pa	v_h	0.3
R_h	70 mm	E_d	9×10^8 Pa
v_d	0.4	R_d	72 mm
k_p	1×10^4 kN/m	k_a	1.1×10^4 kN m/rad
$\mu_1, \mu_2, \mu_3, \mu_4, \mu_5, \mu_{hd}$	0.19, 0.19, 0.25, 0.2, 0.2, 0.15		

4.1. Dynamics of Multiple Vibration Suppression

To demonstrate the theoretical analysis of the damping characteristics, taking the pre-tightening force as the control variable, the dynamic responses of multiple vibration suppression of the shaft (we use the sleeve center to represent the shaft segment center at L_h) and ring are investigated in detail. To eliminate the interference of misalignment, the static angular and parallel misalignment is set to 0. The natural frequencies of the two shafts are close to each other, and the first critical speed is delayed due to the restriction of the damping ring. The analysis in this part is at a speed that is slightly later than the natural frequency.

A sufficiently large pre-tightening force of $F_{pr} = 200N$ is set to make the damper work in the 1st stage and make the ring stationary. The response in the dynamics of shaft 1 and shaft 2 is shown in Figure 9. Due to the different impact stiffnesses around the ring, as shown in Table 1, its displacement orbits are similar to one closed circle with slight deformation. Almost no amplitude fluctuations appear in the time-domain waveform. All of them indicate that synchronous full annular rub impact has occurred.

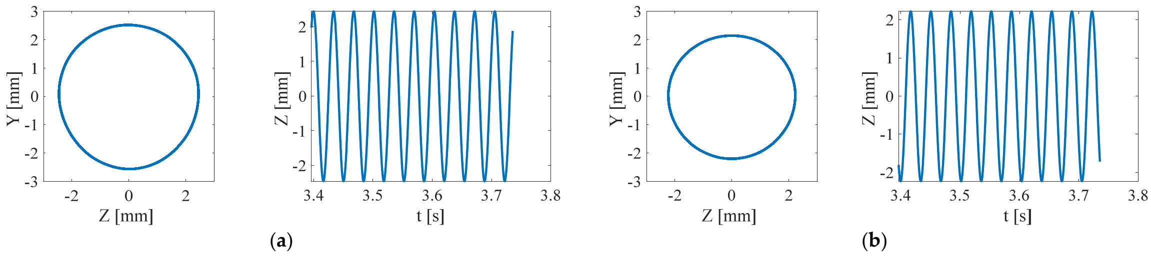

Figure 9. Displacement orbits and time-domain waveforms at the *Z*-axis of (**a**) shaft 1 and (**b**) shaft 2, $F_{pr} = 200N, 1.08\omega_{n1}$.

Reducing F_{pr} to 110 N, Figure 10 illustrates the response of two shafts as well as two dampers. The orbits of the two shafts are similar to an annulus with deformation, but the rub impact of shaft 2 is more serious, which can also be seen from the frequency spectrum. Several points converge in the Poincaré map. The orbits of two rings are similar to polygons whose maximum amplitudes are less than the gaps $\delta_{1,\mathrm{II}}$ and $\delta_{2,\mathrm{II}}$, so both dampers work in the 2nd stage. The eccentric signal component, which is harmonic with the rotating frequency (1×) in shafts, is dominant, while the other components are not obvious. The spectrum of the ring has superharmonic orders (2×, 3×, and 4×). Amplitude fluctuations in the time−domain waveform of the ring are more serious than those in the shaft. All these results demonstrate that the damper is more greatly affected by the rub impact force than the shaft.

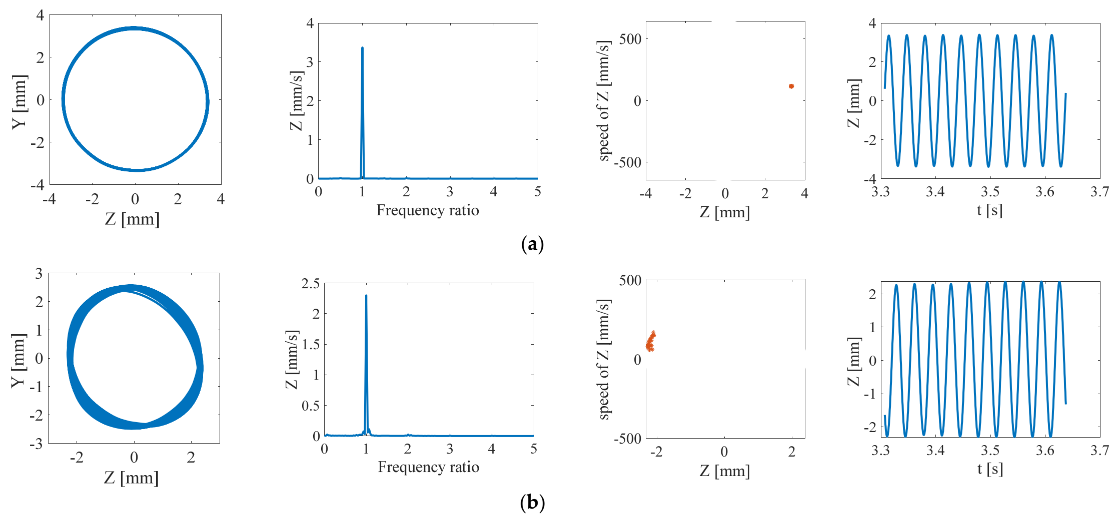

Figure 10. *Cont.*

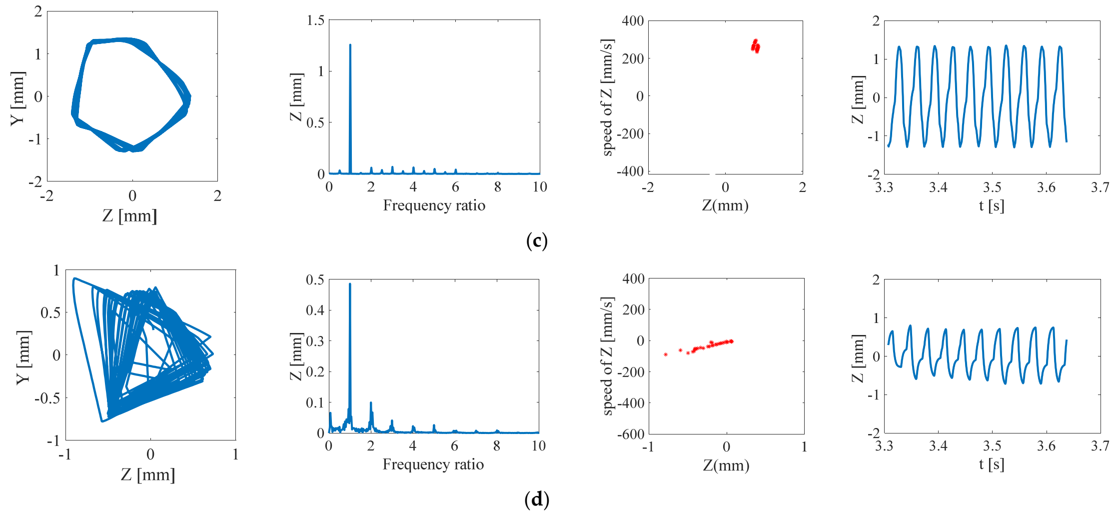

Figure 10. Displacement orbits, frequency spectrum, Poincaré map and time-domain waveform at the *Z*-axis: (**a**) shaft 1, (**b**) shaft 2, (**c**) damper 1, and (**d**) damper 2, $F_{pr} = 110N, 1.08\omega_{n1}$.

Further reducing the pre-tightening force will enlarge the maximum amplitude of the shaft and the ring, which is greater than the gap $\delta_{1,B}$. Therefore, damper 1 works in the 3rd stage, as displayed in Figure 11a. Due to the small eccentricity of shaft 2, damper 2 still works in the 2nd stage, as displayed in Figure 11b. It is noteworthy that the norm of the displacement vector, namely, the amplitude of the sleeve and ring, has a relationship $\left|(\mathbf{\Phi}_{h1} - \mathbf{\Phi}_{\mathbf{d1}})\mathbf{Q}\right| \approx \delta_{1,A}$, which signifies that the phase difference between them is approximately equal to 0. Compared with the irregular orbits in the 2nd stage as shown in Figure 10, the dampers return to a circular ring, which implies that their chaotic behavior has been reduced.

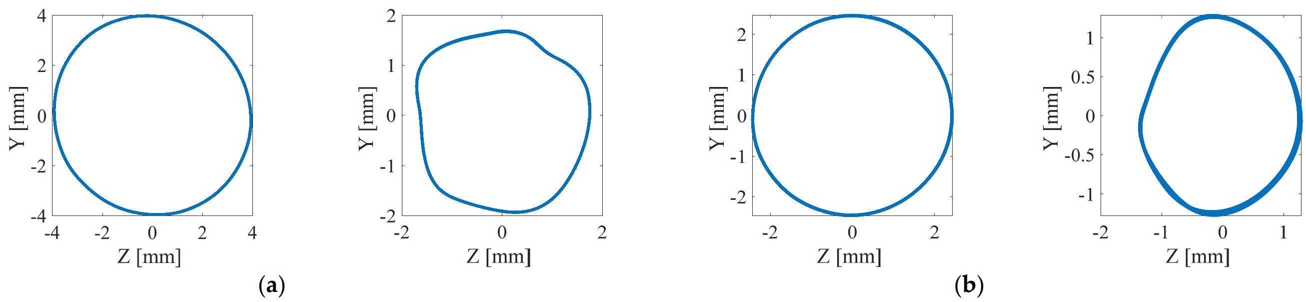

Figure 11. Displacement orbits and frequency spectra of (**a**) shaft 1 and shaft 2, (**b**) damper 1 and damper 2, $F_{pr} = 20N, 1.08\omega_{n1}$.

A more chaotic response appears in shaft 2 than in shaft 1. Accordingly, the chaotic degree of damper 2 is larger than that of damper 1. Since the damping ring contains a self-lubricating material, the low friction coefficient on the surface results in a relatively stable periodic solution compared with the rub impact in the traditional rotor-stator. Both damper 1 and damper 2 are approximately in full annular rub in the 1st and 3rd stages, while they are in partial rub in the 2nd stage. In ref. [33], the intermittent contact caused by partial rub leads to greater wear. Therefore, adjusting the pre-tightening force not only improves the damping performance but also ameliorates the wear property.

The vibration response of the shaft is output by multi-mode superposition as Equation (34). This is one of the differences between this paper and ordinary rotor/stator response. Ordinary rub impact model [7,8] lumps the mass in middle. While in this work, the shaft with mass, elasticity, and internal damping distribution of shaft is considered. In addition, the motion of the stator, that is, the damping ring, is not considered in the ordinary rub impact model. In this work, the motion of the shaft, as well as the damping ring and the stiffness provided by itself are taken into account.

With increasing speed, the amplitude of the shaft is sufficient enough to contact the ring, as depicted in Figure 12. The rub-impact occurs at p 1 with a damping effect to restrict the upsurge of the amplitude, seen from the change in the curve slope. The damper is motionless, namely, it is in the 1st stage and the first rub-impact. The amplitudes of the shaft and damper increase slowly along with the impact until the spring preload is insufficient to restrict the ring. Afterward, it starts to move with amplitude uprush since the speed increases after breaking through static friction (>sliding friction), corresponding to p 2 (enters the 2nd stage). Then, the amplitude of damper 1 reaches $\delta_{1,B}$ and is maintained since the chamfer on the sleeve clings to the fillet on the plate. $\left|(\mathbf{\Phi}_{h1} - \mathbf{\Phi}_{\mathbf{d1}})\mathbf{Q}\right| > \delta_{1,A}$, and the amplitude of shaft 1 continues to increase due to the elastic deformation of the ring. After that, bushing overcomes the spring preload from the plate, and it enters the 3rd stage (p 3) with amplitude uprush, the second rub impact interacts with the first rub impact (r2 & r1). After exceeding the critical speed, the phase difference between eccentric excitation and the response changes from positive to negative. The decrease in energy leads to a jump (p 4) from the 3rd stage to the 2nd stage, followed by another jump (p 5) from continuous rub impact to the separation of the sleeve and the ring. The shaft returns to periodic motion. The numerical simulation results demonstrate the accuracy of the theoretical analysis of multiple vibration suppression. The analytical model developed in this work can reflect the practical system. The natural frequency of shaft 2 is larger than that of shaft 1, and the rotation speed at the beginning of damping is also larger. The vibration suppression of the two dampers is not synchronized in the same parameter settings, resulting in different stages at the same speed. Due to the difference in eccentricity, the maximum amplitude of shaft 2 is not as large as that of shaft 1, and damper 2 does not enter the 3rd stage, the interaction of the first and second rub-impact won't happen. Therefore, the vibration reduction effect of shaft 2 is better under the same spring preload. The amplitudes of damper 2 and shaft 1 also increase in steps and decrease in steps. These stage changes involve the condition transformation of the two shafts mentioned in Equation (41), accompanied by the changes of the degree of freedom and the rub impact equation, especially in the dual rub impact, the interaction of the shaft, damping ring, and plate have a transfer relationship. As a result, the classical method for solving rotor dynamics is not applicable in this example, only the improved Adams–Bashforth can meet the requirements of accuracy and speed.

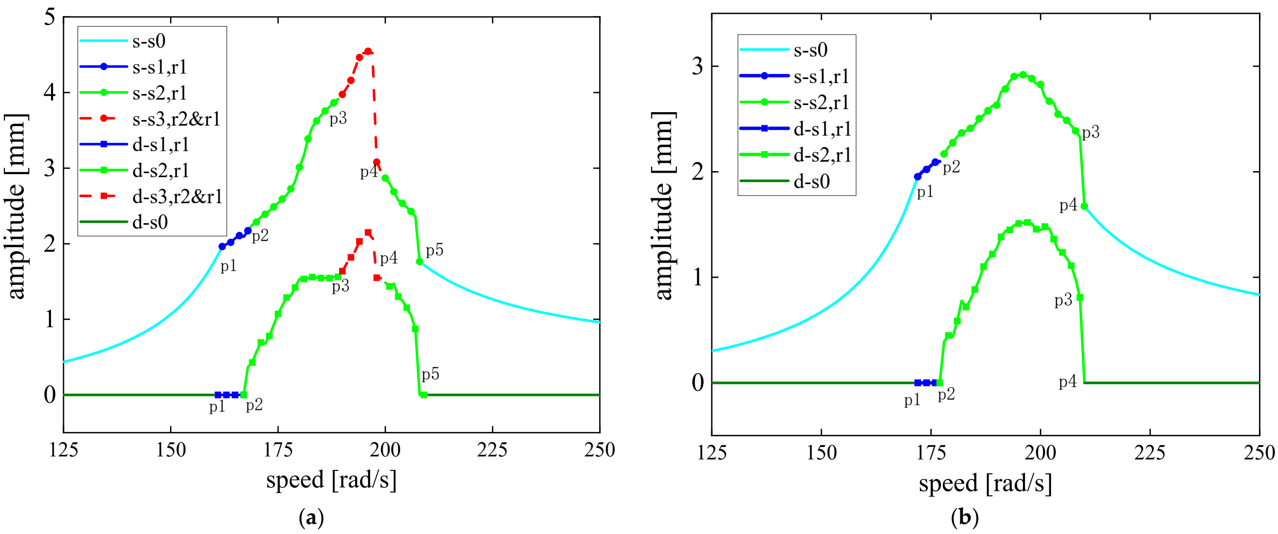

Figure 12. The amplitudes of (**a**) shaft 1 and damper 1 and (**b**) shaft 2 and damper 2, $F_{pr} = 20\ N$. (s−shaft, d−damper, s0—no contact stage, s1—the 1st stage, s2—the 2nd stage, s3—3rd stage, r1—the first rub−impact, r2—the second rub−impact).

As mentioned above, the motion of the stator (damping ring) is involved, the rub impact motion, which is composed of the two mutual motions, can be independent of each other when they are separated, forming different bifurcation degrees. Increasing the pre-tightening force can improve the damping capacity, but the bifurcation of the system is also more serious. Setting $F_{pr} = 110N$, bifurcation diagrams of shaft 1, damper 1, shaft 2 and damper 2 in the Z-axis direction varying with rotating speeds from 100 to 300 rad/s (955–2895 rpm) are depicted in Figures 13 and 14. In the 1st stage, the shaft still has a periodic solution. The damper has one point at one speed, and these points do not form a line. It can be understood that the impact force is not enough to maintain the ring's continuous movement, so the damper works between the 1st and 2nd stages. With increasing speed, it converts to the 2nd stage (p 2), and then the dynamic behavior of the shaft and damper bifurcate into chaotic motion. Even if the damper is more greatly affected by rub impact than the shaft, it does not enter chaos through a period-doubling bifurcation cascade as the common rotor-stator, due to the low friction coefficient on the surface of the damping ring. At the end of the rub impact, the trajectory of the damper exhibits scattered points again.

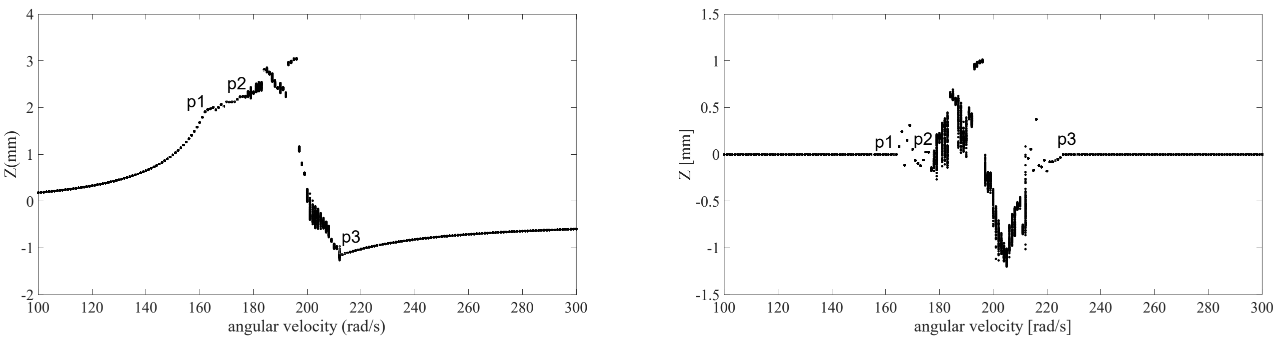

(**a**) (**b**)

Figure 13. Bifurcation diagrams of (**a**) shaft 1 and (**b**) damper 1 in the Z-axis direction, $F_{pr} = 110N$.

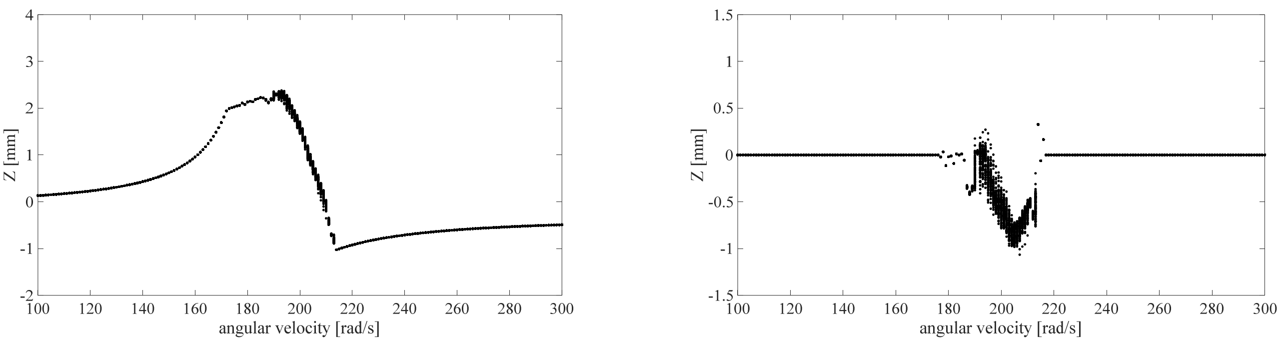

(**a**) (**b**)

Figure 14. Bifurcation diagrams of (**a**) shaft 2 and (**b**) damper 2 in the Z-axis direction, $F_{pr} = 110N$.

4.2. Misalignment Effect of Flexible Diaphragm Coupling

4.2.1. Angular and Parallel Misalignment

It is found that eccentricity is the dominant component of the response signal at the critical speed. The misalignment has a greater impact on the system response far away from the critical speed, where the amplitude is less than the clearance $\delta_{1,\mathrm{I}}, \delta_{2,\mathrm{II}}$; then, the influence of rub impact can also be eliminated. The vibration responses of two shafts with flexible diaphragm couplings subject to static and dynamic misalignment at speeds close to $5\omega_{n1}/6$ are depicted in Figures 15–17.

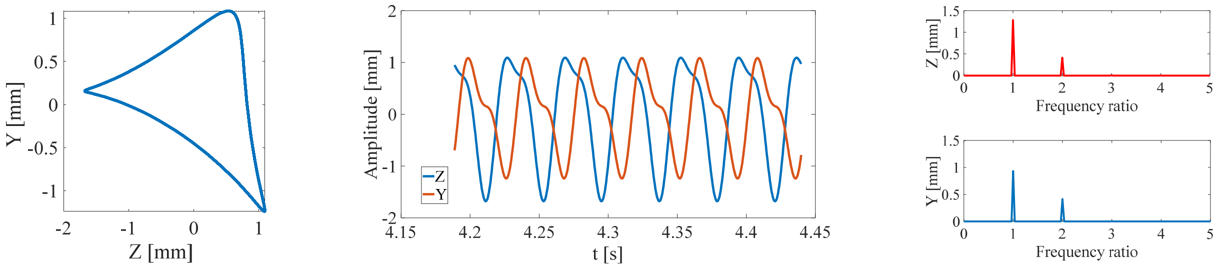

Figure 15. Vibration with parallel misalignment $v_i = 0.1$ mm, $w_i = 0.2$ mm of shaft 1 at $5\omega_{n1}/6$.

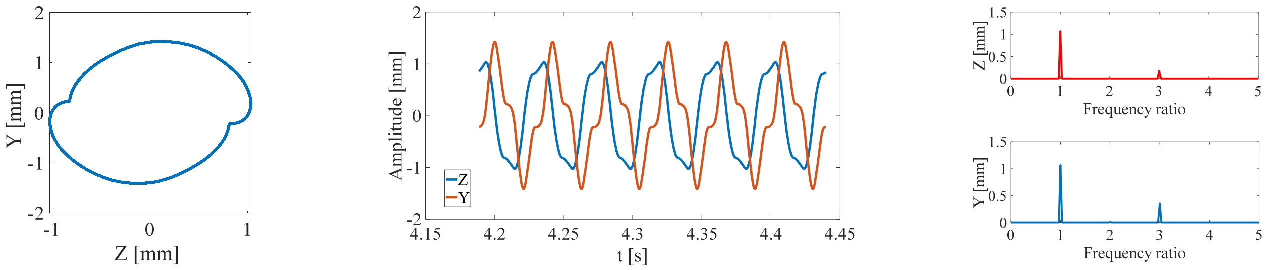

Figure 16. Vibration with angular misalignment $\vartheta_{Zi}= 0.005$ rad,$\vartheta_{Yi}= 0.01$ rad of shaft 1 at $5\omega_{n1}/6$.

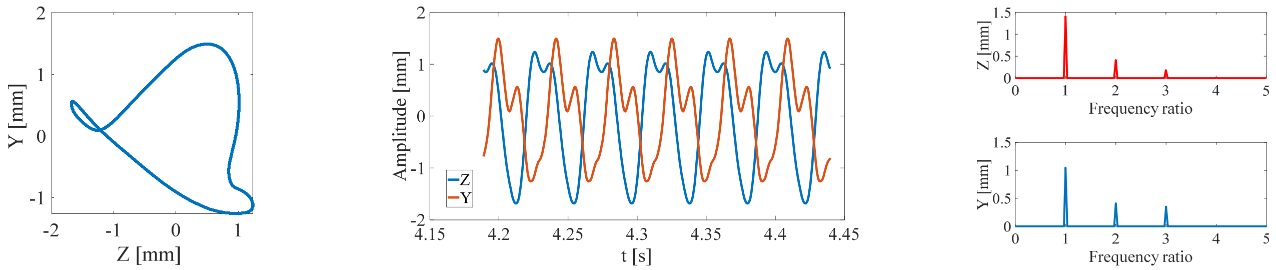

Figure 17. Vibration with angular and parallel misalignment $v_i = 0.1$ mm, $w_i = 0.2$ mm and $\vartheta_{Zi}= 0.005$ rad,$\vartheta_{Yi}= 0.01$ rad of shaft 1 at $5\omega_{n1}/6$.

Figure 15 shows triangle displacement orbits and superposition of the trigonometric functions in the time-domain waveform. Its frequency spectrum illustrates that only the 1st and 2nd harmonic frequencies appear when there is only parallel misalignment, and the magnitude of the second harmonic component in both directions is the same even if the parallel misalignment in the Z-axis is larger. Angular misalignment resulted in the 3rd harmonic frequency, as shown in Figure 16. The angle around the Z-axis is twice that around the Y-axis, which brings about twice harmonic component. Angular misalignment and parallel misalignment usually coexist in practice. This effect is shown in Figure 17. The displacement orbits present an '8' shape. The frequency spectrum is the superposition of those in Figures 15 and 16. This indicates that the two effects are not intercoupling with each other. The misalignment effect is more severe in shaft 2 since its eccentricity is smaller than that of shaft 1, but its response characteristics are similar to those of shaft 1. The above characteristics caused by misalignment can also be inferred from Equations (14) and (23).

Figure 18 shows subcritical harmonic resonance. When the rotating speed of the shafts reaches $\omega_n/3$, the vibration of the two shafts is excited by an angular misalignment force whose frequency is exactly equal to ω_n, as shown in Equation (23). Therefore, the $3\times$ component is much larger than the $1\times$ and $2\times$ components. Its displacement orbits are similar to three elliptic loops. Similarly, if the speed reaches $\omega_{n1}/2$, resonance is excited by a $2\times$ parallel misalignment force, as shown in Figure 18b.

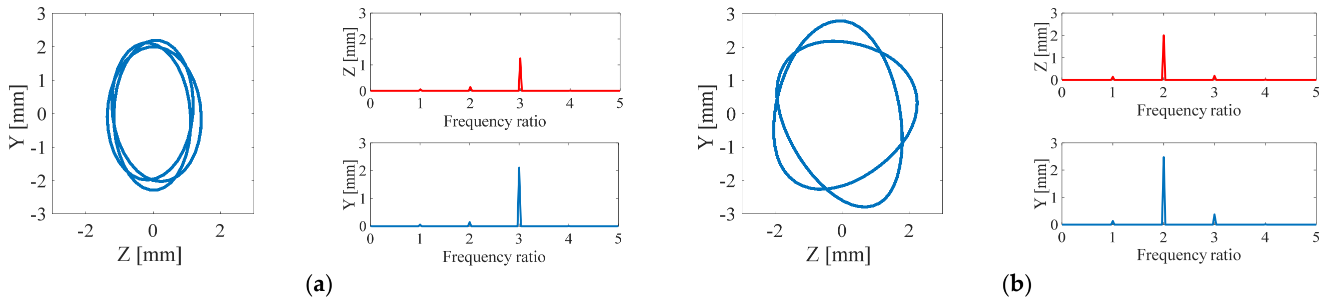

Figure 18. Resonance of shaft 1 at (**a**) $\omega_{n1}/3$ and (**b**) $\omega_{n1}/2$ due to parallel and angular misalignment with $v_i = 0.2$ mm, $w_i = 0.4$ mm and $\vartheta_{Zi}= 0.007$ rad, $\vartheta_{Yi}= 0.014$ rad.

4.2.2. Static Misalignment

Assuming that two shafts connected by coupling are rigid and do not produce dynamic deflection, there is only static misalignment. The response conducted by static misalignment is displayed in Figure 19.

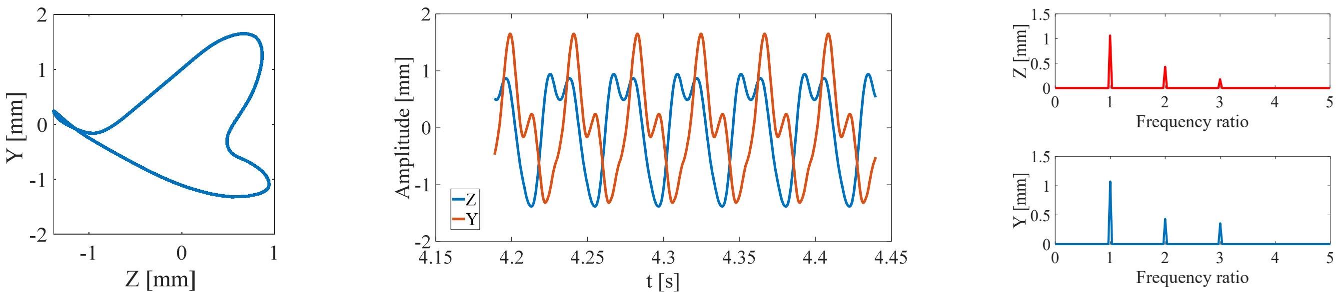

Figure 19. Vibration with static angular and parallel misalignment for shaft 1 at $5\omega_{n1}/6$.

It is found that there is no wide difference between static misalignment and dynamic misalignment by comparing Figures 17 and 19 in this system. This is due to the mode of the shaft near the first critical speed, resulting in a small dynamic offset at both ends of the shaft. The amplitude in Figure 17 is smaller than that in Figure 19. The vibration energy is relatively small when there is only static misalignment. The characteristics of static misalignment are also described in ref. [31]. If the dynamic misalignment is set to 0 in Equations (10) and (16), a flexible coupling model suitable for static misalignment can be obtained.

Compared with the proposed model with only static misalignment [31,32] or angular misalignment [29,30], this model takes dynamic misalignment caused by the offset of the flexible shaft during rotation and static misalignment into account, covers the cases of parallel and angular misalignment. Therefore, it provides a more accurate, comprehensive and universal framework.

4.3. Coeffect of Misalignment and Vibration Suppression

The system will produce a complex vibration response under forces from rub impact, eccentricity, restriction on the damping ring, and angular and parallel misalignment when misalignment and vibration suppression coexist. This coeffect is analyzed and shown in Figure 20.

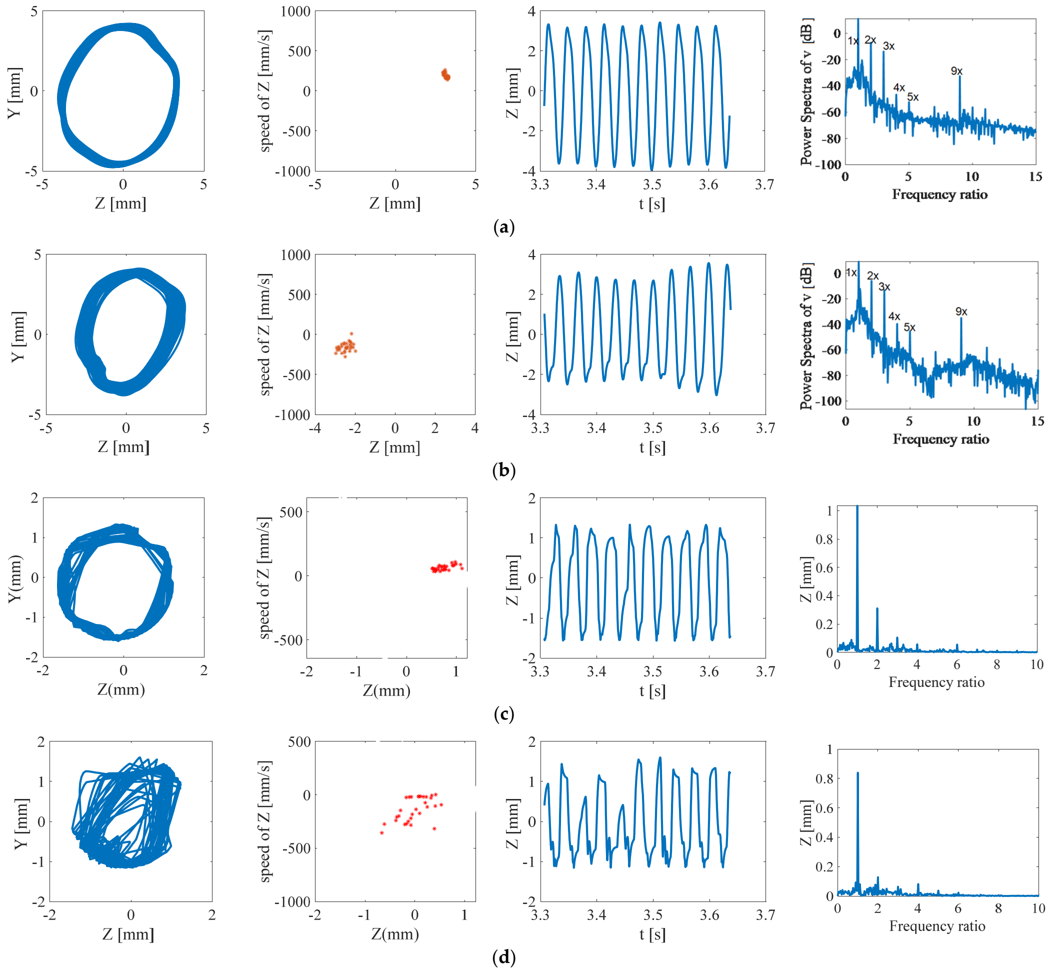

Figure 20. Displacement orbits, Poincaré map and time-domain waveform, power spectrum or frequency spectrum at the *Z*-axis for (**a**) shaft 1 (**b**) shaft 2 (**c**) damper 1 and (**d**) damper 2, where $F_{pr} = 200N$, $v_i = 0.1$ mm, $w_i = 0.2$ mm, $\vartheta_{Zi}= 0.007$ rad,$\vartheta_{Yi}= 0.014$ rad at $1.08\omega_{n1}$.

The rub-impact situations with and without misalignment are compared, i.e., Figures 9 and 20. The former is in the 1st stage, and the latter is in the 2nd stage. This illustrates that misalignment enhances the vibration energy of the system at resonance, and the same pre-tightening force can no longer limit the static state of the damping ring. Misalignment also aggravates rubbing between the sleeve and damping ring, whose displacement orbits change from a single loop to annuluses, and the Poincaré map reveals more scattered points. The power spectrum demonstrates the rub-impact and misalignment motion of the shaft, as marked by clear peaks. In the damper, this coeffect results in an irregular time-domain waveform and abundant components of frequency not only in $2\times-$ and $3\times-$ order but also in other orders. The general research always regards the stiffness around the stator as the same, because they only care about the local surface stiffness. Another contribution of this paper is that deformation properties of the stator (the damping ring) are involved in the rub impact stiffness to provide practical situation. The difference in the anti-deformation stiffness along the damping ring can be clearly shown in Figure 20d. The bottom stiffness is large, and the curve in the bottom is close to the circle, which is also reflected in Section 3.2.2.

The misalignment, coexistence of rub impact and misalignment, and misalignment occur in order in the process from start-up to spanning the first critical speed. The waterfall diagram of the process is analyzed in detail. The case of shaft 2 is similar to that of shaft 1, which will not be repeated.

The response in the case of only rub impact from vibration suppression is shown in Figure 21. Shaft 1 presents a relatively stable periodic solution under eccentric dominance. There are obvious integer order and non-integer order frequencies in damper 1 in all rub-impact processes. The restraining force on the damping ring is always counteracted by the rub-impact force in the 2nd stage, which indicates that these frequency components are exactly caused by rub impact.

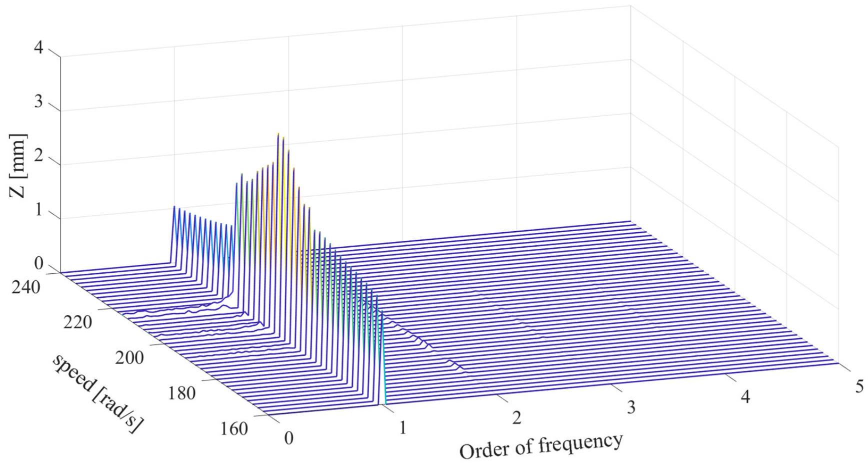

(**a**)

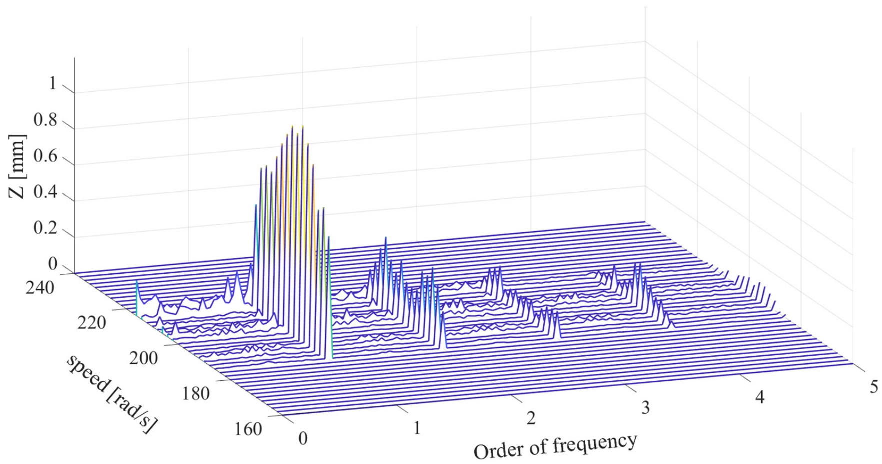

(**b**)

Figure 21. Waterfall plot of the vibration suppression of (**a**) shaft 1 and (**b**) damper 1 for $F_{N0} = 200N$.

In the case of the only misalignment, $1\times$, $2\times$, and $3\times$ frequencies are predominant, as displayed in Figure 21. Especially at low speed, the proportion of misalignment is larger because the eccentricity at this speed is insignificant. Resonances also appear at speeds of $\omega_{n1}/3$, $\omega_{n1}/2$ due to misalignment and eccentricity, as marked with red rings in Figure 22. This can be mutually verified with Figure 18.

The response in the case of coexistence of rub impact and misalignment is depicted in Figure 23. Compared with the only misalignment in Figure 22, the vibration peak of the shaft is delayed by the restriction of the damper. Compared with only rub impact in Figure 21a, the proportion of misaligned signal components (relative to $1\times$) of the shaft increases, and $2\times$ is obviously amplified. At the same time, the degree of rub impact is more significant, especially in the damper, compared with Figures 21b and 23b. The remarkable feature is displayed in Figure 23b. Abundant non-integer orders appear in the damper at the beginning and end of the vibration reduction process. In view of the findings above, rub impact and misalignment can stimulate each other and increase their components. This leads to more serious rub impact and lower system stability, resulting in more irregular orbits of the shaft and damper.

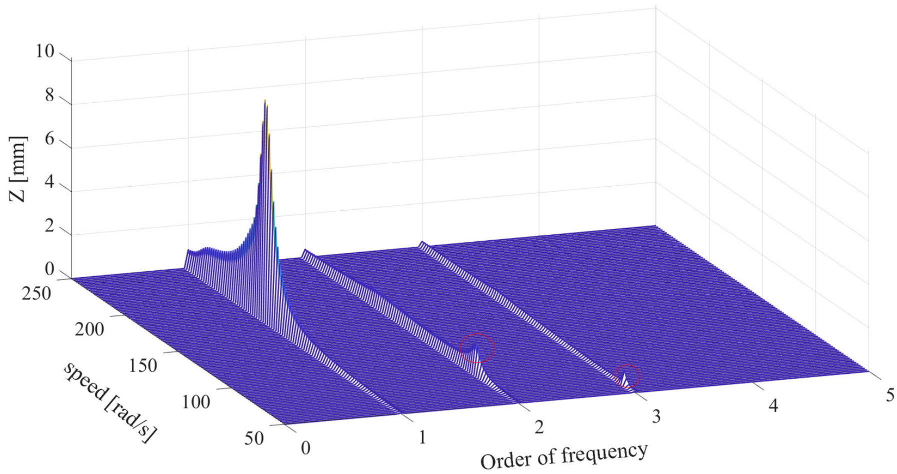

Figure 22. Waterfall plot of the misalignment of shaft 1 for $v_i = 0.1$ mm, $w_i = 0.2$ mm ϑ_{Zi}= 0.005 rad,ϑ_{Yi}= 0.01 rad.

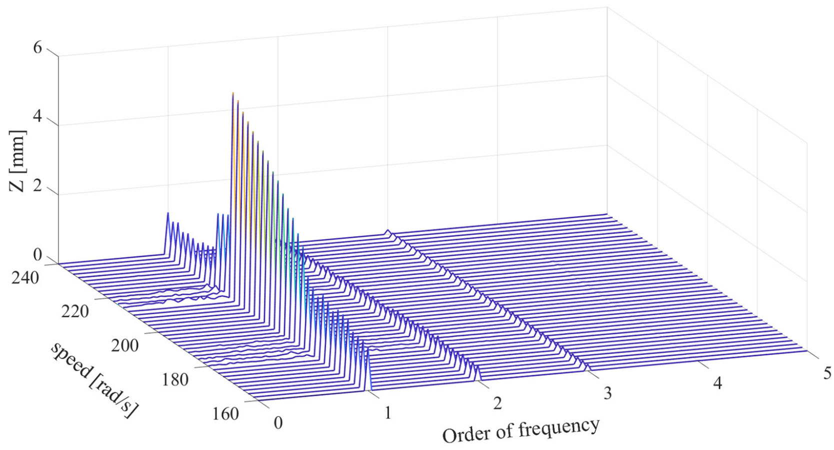

(**a**)

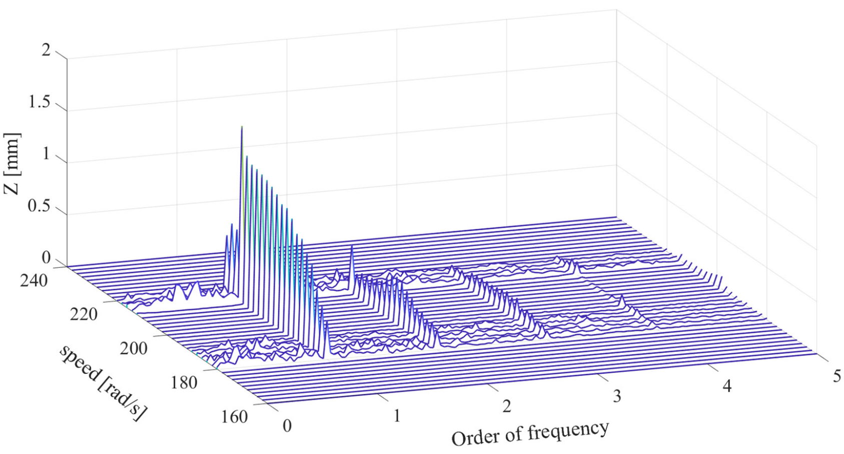

(**b**)

Figure 23. Waterfall plot of the coeffect of misalignment and vibration suppression of (**a**) shaft 1 and (**b**) damper 1 for $v_i = 0.1$ mm, $w_i = 0.2$ mm ϑ_{Zi}= 0.005 rad,ϑ_{Yi}= 0.01 rad $F_{N0} = 200N$.

5. Experimental Verification

There are two purposes for conducting the experiments in this work: the first purpose is to demonstrate the theoretical analysis of the dynamic model of the system, and the second is to verify the response characteristics. A test rig composed of two major shafts, two minor shafts, two dry friction dampers, some discs, a foundation, a motor, brakes, couplings, bearing blocks, sensors, acquisition devices and a computer, is designed to approach the helicopter tail rotor driveline in accordance with the principle of similarity, as shown in Figure 24 and Table 3. Eccentricity is added on the discs, whose weight is relatively small compared with the common rotor test rig to make the modes of the major shaft close to those in practice. The gasket is placed on the bottom of the bearing housing to achieve misalignment of the two major shafts. The dry friction damper is equivalent to the mini version of the original damper with the same material composition and processing technology ring to ensure the same function and key structure to the greatest extent.

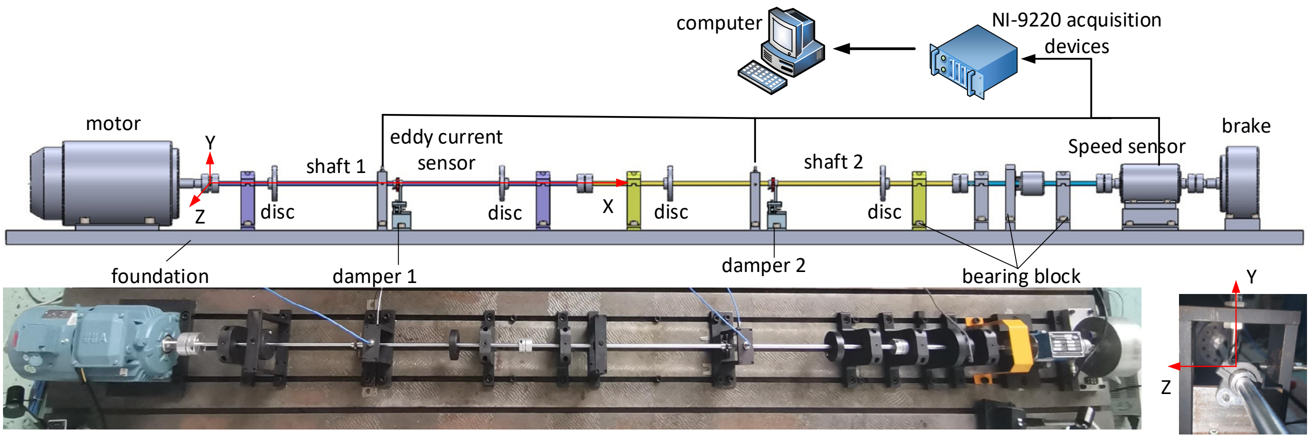

Figure 24. Test rig of the helicopter tail rotor driveline.

Table 3. Parameters of the components.

Components	Material Composition	Value
Shaft 1 and shaft 2	steel	Φ10 × 700 mm, Φ10 × 1000 mm, elastic modulus 211 GPa, Poisson's ratio 0.31, and internal damping 0.001 N s/m
Disc and sleeve	steel	Φ78 × 34 mm, Φ16 × 20 mm,
Hexagon diaphragm coupling	steel	8×10^4 N/m 6×10^4 N m/rad
damping ring	graphite, POB and PTFE	R 16.2 × T 3.6 × W 5.2 mm
Bearing		Left and right: stiffness 40 kN/m, damping 25 N s/m
Unbalance in the disc		Left and right: 2.5 g, eccentricity distance 35 mm
motor and control		constant acceleration from 10 to 2000 rpm in 20 s

Experimental tests were conducted on the test rig with a 1×10^4 Hz sampling frequency, and the results of the data analysis are shown in Figure 24.

After setting the angular and parallel misalignment and dismantling the dampers, $2\times-$ and $3\times-$ order frequency components appear in the waterfall display, as shown in Figure 25a. Before the first critical speed, resonance occurs at $\omega_n/3, \omega_n/2$. After installing dampers and removing the misalignment gaskets, vibration is reduced to a smaller range, slightly greater than the clearance value (0.1 mm), as shown in Figure 25b. A small number of super harmonic orders (2×, 3×, and 4×) are caused by rub impact, presenting only during the first critical speed. Finally, the response under misalignment and damping is depicted in Figure 25c. Compared with Figure 25a, its $2\times-$ and $3\times-$ order components are significantly larger, especially in the first critical speed stage, as marked by the red areas. Compared with Figure 25b, more abundant components appear in the 4× and 5× orders. Non-integer order signal components appear at the beginning and end of the vibration reduction process. The characteristics of these experimental responses are similar to the simulation results, which demonstrate the accuracy of the dynamic model and simulation above.

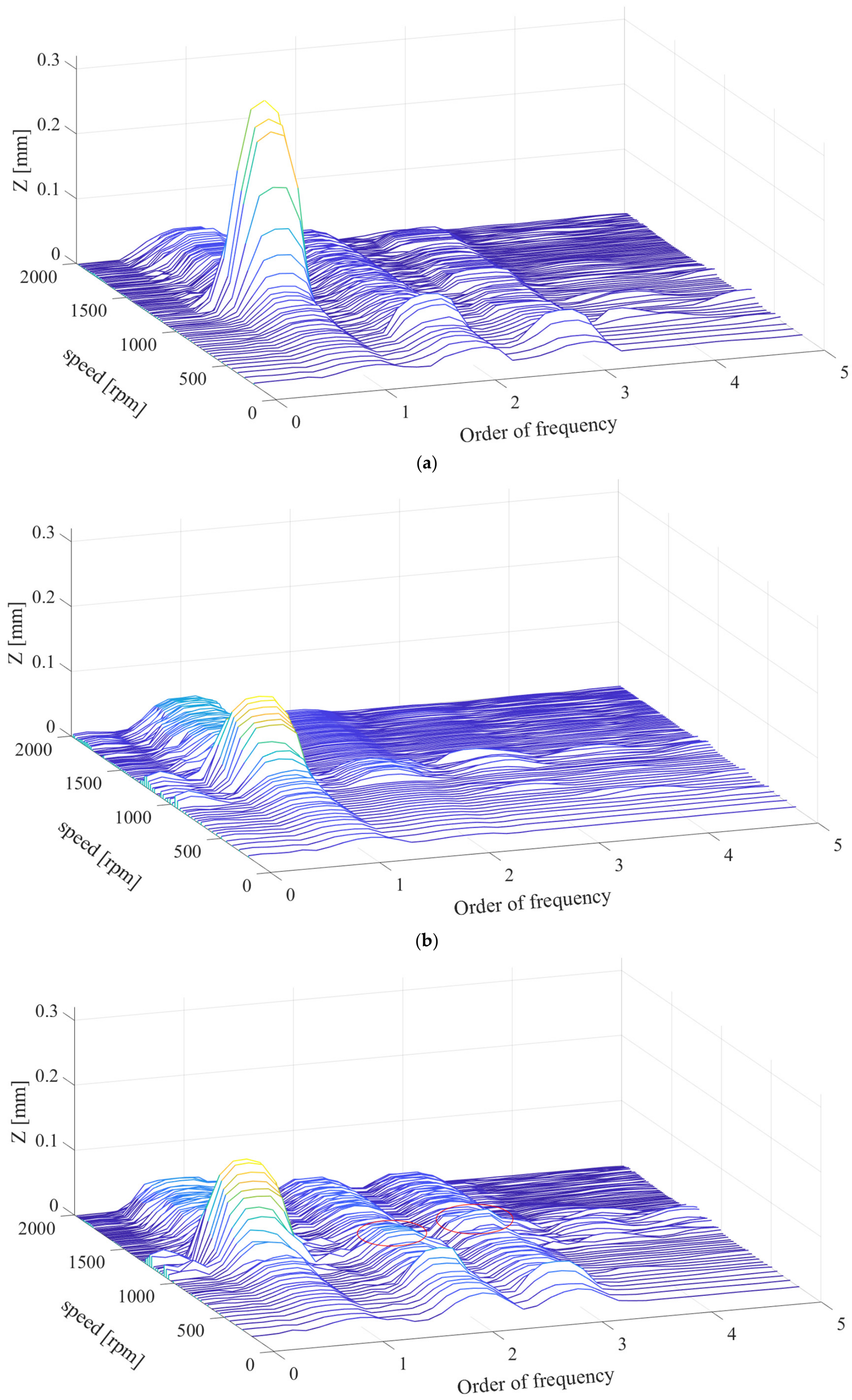

(c)

Figure 25. Waterfall plot of (**a**) misalignment, (**b**) vibration suppression, and (**c**) coeffect of misalignment and vibration suppression from the *Z*-axis direction of shaft 2.

6. Conclusions

This work aims to provide a model foundation and theoretical support for the analysis of the parameter configuration of the helicopter tail drivelines. To this end, a dynamic model of the system consisting of the shaft with continuous internal damping, elasticity and mass distribution, the flexible diaphragm coupling subject to parallel and angular misalignment, and the dry friction damper characterized by multiple stages with transfer conditions and variable DOFs is established. Numerical simulations are carried out by the improved Adams–Bashforth method, in which the calculation accuracy and speed are comprehensively considered. The experimental results demonstrate the accuracy of the dynamic model and simulation. The following valuable phenomena have been revealed:

(1) The vibration response in every vibration suppression stage is analyzed. The vibration suppression of the two dampers is not synchronized for the same parameter settings. Single rub impact occurs in the 1st and 2nd stage, dual rub-impact with interaction occurs in the 3rd stage. The amplitudes of shaft 1, shaft 2, damper 1, and damper 2 have step increases and step decreases. Full annual rub between the sleeve and damping ring occurs in the 1st and 3rd stages, while partial rub occurs in the 2nd stage. The amplitude bifurcation spanning the critical speed indicates that the transformation conditions are consistent with the theoretical analysis. The analytical model developed in this work can reflect the practical system. Even if the damper is more greatly affected by rub impact than the shaft, the degree of chaos is mild due to the low friction coefficient on its surface.
(2) Parallel misalignment and angular misalignment result in 2nd and 3rd harmonic frequencies, respectively. In addition, they are not intercoupled with each other. Resonances also appear at the $1/3$, $1/2$ first critical speed due to misalignment. The vibration energy in the case of only static misalignment is smaller than that coexisting of static and dynamic misalignment, but the characteristics are similar.
(3) In the case of the coexistence of rub impact and misalignment, both of them can stimulate each other and increase their components relative to the eccentricity. However, misalignment still accounts for most of the frequency spectrum of the shaft. In addition, more severe instability and more serious rub impact can be demonstrated from more high-frequency components appearing in the damper.

Author Contributions: Conceptualization and project administration, J.T.; methodology, software, validation and writing, Z.H.; formal analysis and investigation, C.L.; funding acquisition, X.L. and J.T. All authors have read and agreed to the published version of the manuscript.

Funding: This research was funded by the National Key Research and Development Program of China, grant number 2018AAA0101703.

Institutional Review Board Statement: Not applicable.

Informed Consent Statement: Not applicable.

Data Availability Statement: All data generated or analyzed during this study are included in this article.

Acknowledgments: The authors wish to thank Ministry of Science and Technology of the People's Republic of China for their generous funding by the National Key Research and Development Program of China, grant number 2018AAA0101703, also wish to thanks to China Aviation Powerplant Research Institute for their generous funding by Damping Parameter Design and Wear Analysis of a Dry Friction Damper, grant number KY-44-2019-0089.

Conflicts of Interest: The authors declare that they have no competing interests.

Nomenclature

Nomenclature	
ρ, E	density, elastic modulus
δ	clearance
I	cross-sectional transverse moment of inertia
$T,\ D,\ V$	kinetic, dissipation, and strain energy
K	stiffness
J	lumped inertia
L	length
γ	unit pulse function
u, v, w	vibration displacement in X Y Z
$\boldsymbol{F}$	force, vector
F	force, scalar
$\boldsymbol{Q}$	amplitude vector of deflection
N	torque
v	poisson's ratio
c	damping coefficient
ϑ	angular misalignment
Ω , ϕ	rotating speed and rotation angle of the shaft
α	the angle between the tangent of contact point A in the fillet on the plate and the vertical line
φ	the rotation angle of rotating coordinate
ε	the ratio of static friction to dynamic friction coefficient on the surface of the ring
O	center
Φ	modal function
R	radius
θ	the angle around Z-axis
e	eccentricity
Θ	Heaviside function,
m	quality
ω_w	whirling angular velocity of the shaft
μ_{dh}	the friction coefficient between the damping hole and sleeve
d, r_m	the distance from pipe to contact point A and arc radius of the fillet on the plate.
μ_1, μ_2	static friction coefficients between the ring and plate, the ring and base
μ_3, μ_4, μ_5	friction coefficients between bushing and plate, bushing and base, pipe and plate, respectively.
Subscript	
1 or 2	shaft 1 or shaft 2
I, II, III	the 1st, 2nd, 3rd stage
st	static misalignment
cp	coupling
$X\ Z\ Y$	in X, Z, Y direction
r	modal number of the shaft
vi	viscous internal damping
n	bearing block
h	sleeve
rt	in the rotating coordinate frame
s	shaft
d	damper
$N0$	pre-tightening
sp	spring
ϕ	torsion around X-axis
cn	contact
N	normal direction
T	tangential direction
a	angular misalignment
p	parallel misalignment

Appendix A

The ring is assumed to move upward, and the components are represented by solid lines and dotted lines before and after moving, respectively. Enlarging the detailed view of Figure 5, the relationship between the position of each component in the dry friction damper as well as the generated forces in the 3rd stage, as shown in Figure A1.

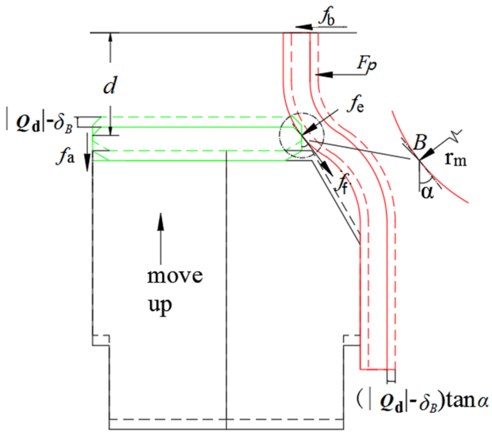

Figure A1. Diagram of movement of components and generated forces.

Firstly, the plate is analyzed separately to meet the equation of

$$\begin{cases} f_c = \mu_3 f_e \\ f_b = \mu_5(f_e \sin\alpha + f_c \cos\alpha) \\ f_b + 2 \times F_N + f_c \sin\alpha = f_e \cos\alpha \end{cases} \tag{A1}$$

The expression of the total spring force F_N after compression is as follows:

$$F_p = F_{pr} + K_{sp}(|\mathbf{Q}_d| - \delta_B) \tan\alpha \tag{A2}$$

Then the force on the bushing in the 3rd stage is expressed as the product of stiffness and displacement in the vertical direction,

$$K_3(|\mathbf{Q}_d| - \delta_2) = (f_f + f_e \sin\alpha) \tag{A3}$$

where

$$f_f = f_a + f_c \cos\alpha = \mu_4(f_e \cos\alpha - \mu_3 f_e \sin\alpha) + \mu_3 f_e \cos\alpha \tag{A4}$$

Combing Equations (A1)–(A4), it gets,

$$K_{\mathrm{III}} = \frac{2\left[F_{N0} + K_{sp}(|\mathbf{Q}_d| - \delta_B)\tan\alpha\right]\left[(\mu_3+\mu_4)\cos\alpha + (1-\mu_4\mu_3)\sin\alpha\right]}{(|\mathbf{Q}_d| - \delta_2)\left[(1-\mu_5\mu_3)\cos\alpha - (\mu_3+\mu_5)\sin\alpha\right]} \tag{A5}$$

where μ_3, μ_4, μ_5 are the friction coefficients between the bushing ring and the plate, the bushing ring and the base, the pipe and the plate, respectively. Furthermore,

$$\alpha = \sin^{-1}\left(\frac{d - (|\mathbf{Q}_d| - \delta_B)}{r_m}\right) \tag{A6}$$

where d, r_m are the vertical distance from pipe to contact point B and arc radius of the fillet on the plate at B.

References

1. Hamann, J.; Kpken, H.G.; Stoiber, D. Drive of a Tail Rotor of a Helicopter. U.S. Patent 9,631,516, 25 April 2017.

2. Shaik, K.; Dutta, B.K. Tuning Criteria of Nonlinear Flexible Rotor Mounted on Squeeze Film Damper Using Analytical Approach. *J. Vib. Eng. Technol.* **2021**, *9*, 325–339. [CrossRef]
3. Bui, Q.-D.; Nguyen, Q.H.; Tien, N.T.; Mai, D.-D.; Nguyen, T.T. Development of a Magnetorheological Damper with Self-Powered Ability for Washing Machines. *Appl. Sci.* **2020**, *10*, 4099. [CrossRef]
4. Mingfu, L.; Mingbo, S.; Siji, W. Active Elastic Support/Dry Friction Damper with Piezoelectric Ceramic Actuator. *Shock Vib.* **2014**, *2014*, 712426. [CrossRef]
5. Khanlo, H.; Ghayour, M.; Ziaei-Rad, S. The effects of lateral–torsional coupling on the nonlinear dynamic behavior of a rotating continuous flexible shaft–disk system with rub–impact. *Commun. Nonlinear Sci. Numer. Simul.* **2013**, *18*, 1524–1538. [CrossRef]
6. Wang, Y.; He, Z.; Zi, Y. A Comparative Study on the Local Mean Decomposition and Empirical Mode Decomposition and Their Applications to Rotating Machinery Health Diagnosis. *J. Vib. Acoust.* **2010**, *132*, 021010. [CrossRef]
7. Wang, Y.; Markert, R.; Xiang, J.; Zheng, W. Research on variational mode decomposition and its application in detecting rub-impact fault of the rotor system. *Mech. Syst. Signal Process.* **2015**, *60–61*, 243–251. [CrossRef]
8. Wang, S.; Yang, L.; Chen, X.; Tong, C.; Ding, B.; Xiang, J. Nonlinear Squeezing Time-Frequency Transform and Application in Rotor Rub-Impact Fault Diagnosis. *J. Manuf. Sci. Eng.* **2017**, *139*. [CrossRef]
9. Hu, A.; Xiang, L.; Zhang, Y. Experimental study on the intrawave frequency modulation characteristic of rotor rub and crack fault. *Mech. Syst. Signal Process.* **2019**, *118*, 209–225. [CrossRef]
10. Tao, Z.; Yian, D.; Fan, H.; Xiangqi, Z.; Yaoyao, W.; Tianlin, L.; Bolchover, P.; Tao, Y.; Guishui, Z.; Rongbing, C.; et al. Reducing Vibration of a Rotating Machine with Deep Reinforcement Learning. In Proceedings of the 2020 IEEE International Conference on Mechatronics and Automation, Beijing, China, 2–5 August 2020; pp. 932–937. [CrossRef]
11. Dai, W.; Mo, Z.; Luo, C.; Jiang, J.; Zhang, H.; Miao, Q. Fault Diagnosis of Rotating Machinery Based on Deep Reinforcement Learning and Reciprocal of Smoothness Index. *IEEE Sens. J.* **2020**, *20*, 8307–8315. [CrossRef]
12. Wang, N.; Jiang, D.; Xu, H. Effects of Rub-Impact on Vibration Response of a Dual-Rotor System-Theoretical and Experimental Investigation. *EXP Tech.* **2019**, *44*, 299–311. [CrossRef]
13. Yang, Y.; Cao, D.; Wang, D.; Jiang, G. Response analysis of a dual-disc rotor system with multi-unbalances–multi-fixed-point rubbing faults. *Nonlinear Dyn.* **2017**, *87*, 109–125. [CrossRef]
14. Han, Q.; Zhang, Z.; Wen, B. Periodic motions of a dual-disc rotor system with rub-impact at fixed limiter. *Arch. Proc. Inst. Mech. Eng. Part C J. Mech. Eng. Sci.* **2008**, *222*, 1935–1946. [CrossRef]
15. Ma, H.; Shi, C.; Han, Q.; Wen, B. Fixed-point rubbing fault characteristic analysis of a rotor system based on contact theory. *Mech. Syst. Signal Process.* **2013**, *38*, 137–153. [CrossRef]
16. Al-Shudeifat, M.A. Stability analysis and backward whirl investigation of cracked rotors with time-varying stiffness. *J. Sound Vib.* **2015**, *348*, 365–380. [CrossRef]
17. AL-Shudeifat, M.A. On the finite element modeling of the asymmetric cracked rotor. *J. Sound Vib.* **2013**, *332*, 2795–2807. [CrossRef]
18. Wang, J.; Ma, L.; Zhang, J.; Lu, X.; Yu, Y. Mitigation of nonlinear rub-impact of a rotor system with magnetorheological damper. *J. Intell. Mater. Syst. Struct.* **2019**, *31*, 321–338. [CrossRef]
19. Xiao, S.; Liu, S.; Wang, H.; Lin, Y.; Song, M.; Zhang, H. Nonlinear dynamics of coupling rub-impact of double translational joints with subsidence considering the flexibility of piston rod. *Nonlinear Dyn.* **2020**, *100*, 1203–1229. [CrossRef]
20. Chen, L.; Qin, Z.; Chu, F. Dynamic characteristics of rub-impact on rotor system with cylindrical shell. *Int. J. Mech. Sci.* **2017**, *133*, 51–64. [CrossRef]
21. Hua, C.; Rao, Z.; Ta, N.; Zhu, Z. Nonlinear dynamics of rub-impact on a rotor-rubber bearing system with the Stribeck friction model. *J. Mech. Sci. Technol.* **2015**, *29*, 3109–3119. [CrossRef]
22. Zhang, W.-M.; Meng, G.; Chen, D.; Zhou, J.-B.; Chen, J.-Y. Nonlinear dynamics of a rub-impact micro-rotor system with scale-dependent friction model. *J. Sound Vib.* **2008**, *309*, 756–777. [CrossRef]
23. Yang, Y.; Wang, Y.; Gao, Z. Nonlinear analysis of a rub-impact rotor with random stiffness under random excitation. *Adv. Mech. Eng.* **2016**, *8*. [CrossRef]
24. Zhang, G.F.; Xu, W.N.; Xu, B.; Zhang, W. Analytical study of nonlinear synchronous full annular rub motion of flexible rotor–stator system and its dynamic stability. *Nonlinear Dyn.* **2009**, *57*, 579–592. [CrossRef]
25. Verma, A.K.; Sarangi, S.; Kolekar, M.H. Experimental Investigation of Misalignment Effects on Rotor Shaft Vibration and on Stator Current Signature. *J. Fail. Anal. Prev.* **2014**, *14*, 125–138. [CrossRef]
26. Browne, M.; Palazzolo, A. Super harmonic nonlinear lateral vibrations of a segmented driveline incorporating a tuned damper excited by non-constant velocity joints. *J. Sound Vib.* **2009**, *323*, 334–351. [CrossRef]
27. Lu, X.; Lu, T.; Zhang, J. Optimization of Geometric Parameters and Stiffness of Multi-Universal-Joint Drive Shaft Considering the Dynamics of Driveline. In *Advances in Evolutionary and Deterministic Methods for Design, Optimization and Control in Engineering and Science*; Springer: Cham, Switzerland, 2019; pp. 445–453.
28. Kang, Y.; Shen, Y.; Zhang, W.; Yang, J. Stability region of floating intermediate support in a shaft system with multiple universal joints. *J. Mech. Sci. Technol.* **2014**, *28*, 2733–2742. [CrossRef]
29. DeSmidt, H.; Wang, K.W.; Smith, E. Stability of a segmented supercritical driveline with non-constant velocity couplings subjected to misalignment and torque. *J. Sound Vib.* **2004**, *277*, 895–918. [CrossRef]
30. Al-Hussain, K. Dynamic stability of two rigid rotors connected by a flexible coupling with angular misalignment. *J. Sound Vib.* **2003**, *266*, 217–234. [CrossRef]

31. Xia, Y.; Pang, J.; Yang, L.; Zhao, Q.; Yang, X. Study on vibration response and orbits of misaligned rigid rotors connected by hexangular flexible coupling. *Appl. Acoust.* **2019**, *155*, 286–296. [CrossRef]
32. Avendano, R.D.; Childs, D.W. One Explanation for Two-Times Running Speed Response Due to Misalignment in Rotors Connected by Flexible Couplings. *J. Eng. Gas Turbines Power* **2013**, *135*, 062501. [CrossRef]
33. Jiang, J.; Ulbrich, H.; Chavez, A. Improvement of rotor performance under rubbing conditions through active auxiliary bearings. *Int. J. Non-Linear Mech.* **2006**, *41*, 949–957. [CrossRef]